Available online at www.sciencedirect.com
ScienceDirect
Icarus 186 (2007) 126–151
ICARUS
www.elsevier.com/locate/icarus

A radar survey of main-belt asteroids: Arecibo observations of 55 objects during 1999–2003

Christopher Magri [a,*], Michael C. Nolan [b], Steven J. Ostro [c], Jon D. Giorgini [d]

[a] *University of Maine at Farmington, 173 High Street—Preble Hall, Farmington, ME 04938, USA*
[b] *Arecibo Observatory, HC3 Box 53995, Arecibo, PR 00612, USA*
[c] *300-233, Jet Propulsion Laboratory, California Institute of Technology, Pasadena, CA 91109-8099, USA*
[d] *301-150, Jet Propulsion Laboratory, California Institute of Technology, Pasadena, CA 91109-8099, USA*

Received 3 June 2006; revised 10 August 2006

Available online 24 October 2006

Abstract

We report Arecibo observations of 55 main-belt asteroids (MBAs) during 1999–2003. Most of our targets had not been detected previously with radar, so these observations more than double the number of radar-detected MBAs. Our bandwidth estimates constrain our targets' pole directions in a manner that is geometrically distinct from optically derived constraints. We present detailed statistical analyses of the disk-integrated properties (radar albedo and circular polarization ratio) of the 84 MBAs observed with radar through March 2003; all of these observations are summarized in the online supplementary information. Certain conclusions reached in previous studies are strengthened: M asteroids have higher mean radar albedos and a wider range of albedos than do other MBAs, suggesting that both metal-rich and metal-poor M-class objects exist; and C- and S-class MBAs have indistinguishable radar albedo distributions, suggesting that most S-class objects are chondritic. Also in accord with earlier results, there is evidence that primitive asteroids from outside the C taxon (F, G, P, and D) are not as radar-bright as C and S objects, but a convincing statistical test must await larger sample sizes. In contrast with earlier work, we find S-class MBAs to have higher circular polarization ratios than other MBAs, indicating greater near-surface structural complexity at decimeter scales, due to different mineralogy (material strength or loss tangent), a different impactor population, or both.

Keywords: Asteroids; Radar observations

1. Introduction

Radar observations offer unique information about the physical properties of asteroids. Since the late 1960s nearly 300 asteroids have been detected via radar, primarily at the Arecibo and Goldstone telescopes. (See http://echo.jpl.nasa.gov/asteroids/index.html for an updated history of these detections.) As discussed by Ostro et al. (2002), radar data can be used to constrain the target's orbit, size, shape, and spin vector, its near-surface roughness at decimeter scales (due to surface rocks, buried rocks, and subsurface voids), and its near-surface bulk density, which can tell us about mineralogy (e.g., metal content—see Ostro et al., 1991) or else about near-surface porosity (Magri et al., 2001).

Several years ago Magri et al. (1999, hereafter Paper I) carried out statistical analyses of the 37 main-belt asteroids (MBAs) that had been detected via radar by 1995. Their goal was to look for similarities and differences in radar properties as a function of Tholen taxonomic class (Tholen and Barucci, 1989; Tholen, 1989). They reached two firm conclusions. First, C- and S-class MBAs have indistinguishable distributions of radar reflectivity (OC albedo), consistent with the idea that most S-class asteroids have chondritic rather than stony-iron composition. Second, M-class MBAs have higher mean radar albedo, and a wider range of radar albedos, than do those in other taxa. This is consistent with the M taxon being a heterogeneous grouping of metal-rich objects (with high radar albedo) and stony (e.g., enstatite) objects (with moderate radar albedo).

* Corresponding author. Fax: +1 207 778 7365.
E-mail address: magri@maine.edu (C. Magri).

0019-1035/$ – see front matter
doi:10.1016/j.icarus.2006.08.018

Paper I also reaches two tentative conclusions: dark MBAs from outside the C taxon (i.e., B-, F-, G-, and P-class objects) might have lower radar albedos than do C- and S-class objects; and M-class MBAs might exhibit an anticorrelation between radar albedo and visual albedo.

In the mid-1990s the Arecibo Observatory underwent a major upgrade, greatly increasing the telescope's sensitivity and doubling the radar transmitter's power. This made it much easier than before to detect MBAs, whose large distances—radar echo power is proportional to the inverse fourth power of the distance—make them quite challenging to detect. Realizing that we could at least double the number of main-belt detections in just a couple of years, we launched a two-year survey at Arecibo beginning in 2000. Early problems with the newly upgraded system eventually stretched the survey out to three years, but we did reach our goal.

Here we present detailed analyses of this enlarged sample. The next section describes our survey observations of 55 MBAs, 46 of which had not previously been observed with radar. Section 3 discusses how we analyzed the data for each target to obtain parameters such as radar albedo and circular polarization ratio. Section 4 presents our statistical analyses of the full 84-object MBA radar data set, and Section 5 summarizes physical implications of our results. Online supplementary information summarizes in one place the pre-upgrade and post-upgrade MBA radar experiments on which our analyses are based.

2. Observations and data reduction

The continuous-wave (CW) spectra discussed here were obtained between September 1999 and March 2003 (see Table 1) at the Arecibo Observatory. For each observation (or "run") of a given target we transmitted a circularly polarized monochromatic signal at about 2380 MHz for a duration almost equal to the round-trip light-time (RTT) to the target, then switched to receive mode for an equal duration, measuring the echo signal in both the same circular polarization as was transmitted (SC) and the opposite circular polarization (OC). Received echoes in each polarization were converted to analog voltage signals, amplified, mixed down to baseband, and filtered; we then took complex voltage samples at rate $\Re$ (usually 50,000 or 62,500 Hz), digitized them, and wrote them to disk for later processing.

It was important to compensate for the Doppler shift due to relative motion between the telescope and the target's center of mass (COM), so as to avoid Doppler smearing produced by changes in this shift over a run's duration. Before each experiment we generated ephemeris predictions of the COM Doppler shift. While transmitting we continuously adjusted the signal frequency so that hypothetical echoes from the COM would return at the desired frequency—say, 2379.985 MHz (see below)—if our ephemeris were exactly correct. For a minority of runs we instead compensated for the COM Doppler shift by leaving the transmitted frequency unchanged and continuously adjusting the center frequency at which we received echo power.

All of our target asteroids have well-constrained orbits and hence precisely known COM Doppler ephemerides; the a priori uncertainty at a given epoch was usually less than 0.1 Hz, much smaller than the Doppler bandwidth (due to target rotation) of even our narrowest echoes (∼4 Hz). Hence it is not surprising that we measured no significant deviations between predicted and observed COM Doppler shift.

Since the echo from the asteroid is usually dwarfed by noise power, we needed a reliable method for removing the noise background from our data. This was accomplished through a frequency-switching observing scheme. For example, during a given run we might use four different frequencies, spaced 10 kHz apart and centered on 2380 MHz, for 10 s each, repeating this cycle every 40 s. (We refer to each 10-s interval as a "dwell.") In other words, during the first dwell we compensated for the COM Doppler shift so that hypothetical echoes from the COM would return at 2379.985 MHz, and during the next three dwells we incremented this desired return frequency in three successive 10-kHz steps, ending the cycle at 2380.015 MHz.

Data processing for each run began by choosing a frequency resolution Δf. We then took the first $\Re/\Delta f$ voltage samples for that run and Fourier transformed them from the time domain to the frequency domain. This frequency spectrum covers the full unaliased Doppler bandwidth, $-\Re/2$ to $+\Re/2$: any signal whose frequency lies within this interval appears in the transformed spectrum at the correct frequency, whereas a hypothetical signal outside the interval would be shifted ("aliased") to a frequency within the interval. Taking the complex square of the transformed data yielded one "look," a single estimate of the Doppler power spectrum. This process was repeated for the remaining data in the run, producing N_{looks} independent estimates. If τ is the integration time (∼RTT) then the total number of voltage samples per run is N_{looks} $(\Re/\Delta f)$; since the total number of samples can also be written as $\Re\tau$, it follows that $N_{\mathrm{looks}} = \tau\Delta f$.

We then could form an incoherent sum of all looks in the first dwell to get an estimate of signal-plus-background-noise power over the corresponding 10-kHz Doppler interval (2379.980–2379.990 MHz), and could separately sum all looks in the *other* three dwells in the cycle to obtain a echo-free background noise power estimate for the same frequency interval. This procedure was then repeated for the other three 10-kHz intervals in the cycle, yielding a total of four signal-plus-background-noise spectra and four background noise spectra.

In past work we subtracted each background noise spectrum from the corresponding signal-plus-background-noise spectrum and then divided by the background noise spectrum to obtain a baselined, normalized estimate of the signal power spectrum. However, background noise spectra have random fluctuations, and division by Gaussian noise yields non-Gaussian fluctuations that are biased to positive values: We overestimate signal power. This bias can approach 0.5 standard deviations of the noise at the fine frequency resolution of some of our spectra. (Since $N_{\mathrm{looks}} = \tau\Delta f$, fine resolution means few looks for a given integration time, and summing few looks results in large noise fluctuations.) So for the present work we instead automatically fit a low-order polynomial to each background noise

Table 1
Observations[a]

Target	UT observing dates	Mean UT rx date	Runs	RA (h)	Dec (°)	Distance (AU)	Δf (Hz)
3 Juno	2002 Feb 6, 8	7.22	2	9.5 (0.03)	4 (0.3)	1.43 (0.003)	10.0
7 Iris	2000 Jan 8, 10–11	9.41	6	9.3 (0.04)	9 (0.0)	1.27 (0.010)	10.0
13 Egeria	2001 Mar 26, 28, 30	28.62	5	12.8 (0.07)	13 (0.0)	1.49 (0.002)	10.0
15 Eunomia	2002 Sep 25	25.10	1	22.8 (0.00)	12 (0.0)	1.26 (0.000)	8.0
22 Kalliope	2001 Dec 16, 18–20	18.25	4	5.4 (0.07)	30 (0.3)	1.65 (0.006)	10.0
23 Thalia	2001 Oct 7, 9, 12	9.77	3	3.0 (0.05)	8 (0.1)	1.60 (0.042)	5.0
25 Phocaea	2002 Jul 9, 11–14	11.96	5	17.9 (0.05)	17 (0.1)	0.95 (0.011)	2.0
28 Bellona	2002 Feb 6, 10	8.29	2	10.6 (0.04)	10 (0.6)	1.43 (0.013)	2.0
31 Euphrosyne	2000 Oct 6, 8, 10	8.15	4	4.2 (0.01)	33 (0.9)	1.83 (0.044)	25.0
36 Atalante	2001 Oct 5, 7, 9, 12	7.20	4	2.6 (0.09)	35 (1.9)	1.04 (0.035)	5.0
38 Leda	2001 Jan 13, 15	13.90	5	5.8 (0.02)	27 (0.2)	1.41 (0.011)	5.0
46 Hestia	2002 Nov 22–23	22.59	2	2.7 (0.01)	12 (0.1)	1.26 (0.005)	1.0
50 Virginia	2001 Jan 12–14	13.27	5	8.4 (0.03)	16 (0.1)	1.67 (0.001)	4.0
53 Kalypso	2002 Feb 6	6.27	1	11.5 (0.00)	5 (0.0)	1.40 (0.000)	1.0
54 Alexandra	2001 Oct 5–6, 12	5.93	4	23.0 (0.06)	9 (0.4)	1.44 (0.054)	10.0
60 Echo	2001 Oct 5, 7, 19	8.78	3	2.1 (0.19)	11 (1.6)	1.25 (0.063)	1.0
66 Maja	2001 Dec 18–19	18.41	2	2.8 (0.00)	20 (0.0)	1.36 (0.008)	5.0
83 Beatrix	2001 Jan 11, 13, 15	13.19	5	8.9 (0.06)	26 (0.3)	1.40 (0.017)	4.0
85 Io	1999 Sep 20	20.24	3	0.9 (0.00)	12 (0.0)	1.27 (0.000)	10.0
88 Thisbe	2000 Aug 25, Sep 9, 14, Oct 7–10	21.18[b]	9	0.0 (0.55)	9 (3.0)	1.49 (0.075)	25.0
101 Helena	2001 Oct 7, 19	9.28	2	0.5 (0.19)	13 (0.4)	1.31 (0.039)	1.0
109 Felicitas	2002 Nov 20	20.12	1	2.9 (0.00)	30 (0.0)	0.93 (0.000)	1.0
111 Ate	2000 Sep 10–12	11.28	6	0.5 (0.03)	10 (0.1)	1.70 (0.012)	2.5
114 Kassandra	2001 Mar 26, 28, 30	28.12	6	11.4 (0.04)	6 (0.4)	1.36 (0.016)	5.0
127 Johanna	2002 Feb 4, 7–8, 10	7.63	4	9.5 (0.10)	28 (0.3)	1.61 (0.003)	5.0
128 Nemesis	2001 Jan 13, 15	14.41	2	6.6 (0.03)	28 (0.1)	1.72 (0.010)	2.0
137 Meliboea	2002 Sep 25, 28, 30, Oct 1	28.63	4	0.1 (0.07)	8 (1.0)	1.63 (0.013)	1.0
145 Adeona	2001 Mar 27, 29	28.22	4	12.8 (0.03)	16 (0.1)	1.50 (0.003)	10.0
182 Elsa	2002 Feb 8–10	9.18	3	10.9 (0.03)	10 (0.2)	1.43 (0.005)	0.2
192 Nausikaa	2000 Oct 7, 9–10	8.33	3	1.9 (0.04)	22 (0.1)	0.85 (0.006)	2.0
198 Ampella	1999 Sep 20	20.14	3	22.6 (0.00)	12 (0.0)	0.93 (0.000)	2.0
211 Isolda	2001 Dec 21	21.04	1	2.7 (0.00)	18 (0.0)	1.78 (0.000)	5.0
216 Kleopatra	1999 Sep 19–20[c]	19.54	5	4.1 (0.01)	20 (0.1)	1.48 (0.010)	10.0
225 Henrietta	2001 Aug 17–23, 25	20.74	8	21.8 (0.08)	13 (1.3)	1.58 (0.003)	5.0
247 Eukrate	2001 Oct 5, 9	6.89	3	1.2 (0.10)	26 (0.7)	1.18 (0.012)	5.0
253 Mathilde	2001 Aug 16, 20	19.00	3	23.5 (0.02)	2 (0.4)	0.99 (0.018)	0.1
266 Aline	2001 Oct 5, 12	7.35	3	1.6 (0.08)	23 (1.0)	1.41 (0.021)	5.0
270 Anahita	2001 Oct 5–6	5.70	2	23.8 (0.01)	4 (0.1)	0.92 (0.004)	2.0
313 Chaldaea	2003 Mar 28	28.13	2	11.1 (0.00)	5 (0.0)	1.07 (0.000)	2.0
324 Bamberga	2000 Sep 10–14	12.40	5	3.2 (0.06)	33 (1.0)	1.11 (0.026)	2.0
336 Lacadiera	2000 Sep 9–12, 14	11.66	9	23.1 (0.08)	4 (0.6)	1.21 (0.006)	2.0
354 Eleonora	2001 Mar 26–27, 29	27.51	4	11.6 (0.03)	21 (0.4)	1.58 (0.015)	25.0
393 Lampetia	2000 Aug 26	26.17	1	22.2 (0.00)	16 (0.0)	0.98 (0.000)	1.0
405 Thia	2002 Feb 3, 6, 9	6.28	3	8.3 (0.10)	2 (0.1)	1.31 (0.002)	5.0
429 Lotis	2002 Sep 25, 27–30	28.10	8	0.7 (0.06)	13 (0.7)	1.31 (0.012)	2.0
444 Gyptis	2002 Sep 27, 29, Oct 1	29.13	3	0.6 (0.05)	7 (0.7)	1.31 (0.001)	10.0
488 Kreusa	2002 Feb 7, 9	8.18	2	10.3 (0.02)	27 (0.3)	1.67 (0.004)	2.0
505 Cava	2001 Jan 11, 15	13.60	3	7.8 (0.07)	28 (0.6)	1.18 (0.007)	5.0
532 Herculina	2001 Mar 28–30	29.31	6	14.9 (0.01)	12 (0.2)	1.43 (0.009)	10.0
554 Peraga	2000 Jan 8, 11	10.32	2	6.1 (0.05)	25 (0.1)	1.11 (0.014)	2.0
622 Esther	2001 Jan 12, 14	13.36	5	6.6 (0.03)	13 (0.3)	1.11 (0.011)	0.4
654 Zelinda	2002 Feb 3–4, 9–10	6.50	4	6.9 (0.07)	8 (1.2)	0.87 (0.036)	2.0
704 Interamnia	2001 Oct 9, 12, 19	13.04	3	0.3 (0.13)	32 (1.2)	1.69 (0.009)	10.0
914 Palisana	2000 Sep 10–12, 14	11.34	5	21.8 (0.06)	37 (0.7)	1.20 (0.010)	2.0
1963 Bezovec	2001 Jan 12, 14	12.90	5	5.5 (0.03)	15 (0.7)	1.00 (0.010)	0.5

[a] All experiments involved transmission at 2380 MHz and reception in both OC and SC polarizations. For each experiment we give the weighted mean receive date; the number of transmit-receive cycles, or runs; right ascension, declination, and distance from Earth at the weighted mean receive date (with the range of values spanned in parentheses); and the raw frequency resolution Δf. We also observed 219 Thusnelda and 407 Arachne, detecting the latter but not the former; since potential errors in the observing procedure lead us to distrust our results, we do not present any data for these two targets.

[b] The weighted mean receive date for 88 Thisbe is 2000 Sep 21.18 UT.

[c] The CW spectra presented here for 216 Kleopatra are independent from the delay-Doppler images obtained in 1999 November and analyzed by Ostro et al. (2000).

spectrum—typically second order or lower, never more than fourth order—and then subtracted and divided by this smooth curve rather than by the background noise spectrum itself. With the bandwidths we use, modern electronics, and the current RFI environment, the baseline shape is smooth except for slight curvature, so it is sufficient to work with a low-order polynomial fit to the background rather than the actual noisy spectrum.

In addition to solving the bias problem discussed above, this modified procedure increases the signal-to-noise ratio (SNR) by a factor of $\sqrt{4/3}$. This factor obtains because the background noise spectrum is the sum of three dwells and hence has $1/\sqrt{3}$ the noise level of the signal-plus-background spectrum; dividing the two spectra therefore increases the r.m.s. noise by a factor of $\sqrt{1+1/3} = \sqrt{4/3}$. The prediction uncertainty on a low-order polynomial fit is generally tiny compared to the noise in the spectrum being fit, so dividing by the smooth fit rather than by the actual background spectrum results in almost no noise increase.

The baseline noise is assumed to be thermal noise due to the receiver electronics, to stray scattering in the telescope optics that allows in some thermal radiation from the ground, and to the 3 K microwave background. The total "system temperature" is roughly 20–30 K, and is measured regularly by comparison with a calibrated reference noise source. This temperature is converted to a noise power by the relation $P_{\rm noise} = kT_{\rm sys}\Delta f$ per frequency channel per look. We used this noise power to calibrate our signal power. For each dwell, we found the system temperature and gain for the pointing direction at the receive time, and also the gain for the pointing direction RTT seconds earlier when the signal was transmitted. (System temperature, gain, and effective area vary significantly with telescope pointing at Arecibo, due to the telescope's unusual optics, but have been tabulated as a function of telescope pointing using known celestial flux standards [generally quasars]. These calibration tables were provided to us by the observatory.) From the radar equation, the received power $P_{\rm R}$ is

$$P_{\rm R} = \frac{P_{\rm T} G_{\rm T} G_{\rm R} \lambda^2 \sigma}{(4\pi)^3 R^4}, \tag{1}$$

where $P_{\rm T}$ is transmitted power, $G_{\rm T}$ and $G_{\rm R}$ are the telescope gain when transmitting and receiving, σ is radar cross section, and R is the Earth–target distance. Since the r.m.s. noise power fluctuation for the mean of $N_{\rm looks}$ looks is $kT_{\rm sys}\Delta f/\sqrt{\tau\Delta f}$, we could equate this to $P_{\rm R}$ and solve for σ, the radar cross section equivalent of one standard deviation of the noise. Thus we could calibrate our spectrum in units of radar cross section ($\rm km^2$).

In this way we obtained four baselined, normalized, calibrated signal spectra for each 40-s cycle, one spectrum per dwell. We took the unweighted mean of these four spectra and the spectra obtained from the next five cycles: a 4-min "block" of data. Finally we took a variance-weighted mean of all blocks in the run. (Simply taking the variance-weighted mean of all *dwells* in the run tends to produce very noisy spectral baselines; we have found empirically that taking unweighted means over 4-min blocks provides the optimal tradeoff between error due to baseline noise and error due to time variation in gain and $T_{\rm sys}$.)

Each spectrum was automatically assigned a signal range slightly wider than the predicted Doppler bandwidth for the target's diameter and rotation period (see Table 2) and an assumed equatorial view. Since this range might be incorrect due to incorrect diameters or periods, to target elongation, or to pole-on viewing, we inspected all spectra by eye and adjusted the signal range when necessary, taking care to err on the side of ranges too wide rather than too narrow. In no case did we need to widen the range by more than a few tens of percent; in a few cases (e.g., 137 Meliboea) we had to narrow the range substantially due to a nearly pole-on view. We then removed a linear baseline, fitting to those portions of the spectrum lying outside the signal range. This explicit baseline subtraction usually changed our signal values by only a few hundredths of a noise standard deviation—a sign that the automatic background removal procedure described earlier worked well.

We were able to obtain more than one run per experiment for most of our targets, so we created a weighted sum of all runs before estimating cross sections and bandwidths. Table 1 lists observational parameters for all 55 targets. The summed spectra are displayed in Fig. 1. Echo power, in units of standard deviations of the noise, is plotted vs Doppler frequency. 0 Hz corresponds to echoes from the center of mass, as predicted by our ephemerides.

3. Data analysis

Our weighted spectral sums were further analyzed in a manner largely identical to that described in Paper I, and we refer the reader to that work for procedural and mathematical details. The first step required is to produce a triaxial ellipsoid model for each target. We recognize that ellipsoids are crude approximations to real asteroid shapes: For example, a model of one of our targets, 216 Kleopatra, has been described as a dog bone (Ostro et al., 2000), while another target, 532 Herculina, has been likened to a toaster (Kaasalainen et al., 2002a). But the approximation should be adequate for our purposes, namely, to estimate $\langle A_{\rm proj}\rangle$, the mean projected area viewed by the radar, and $D_{\rm max}$, the maximum breadth of the pole-on silhouette. The projected area is used in computing the radar albedo (see below). Combining $D_{\rm max}$ with rotation period P tells us $B_{\rm max}(\delta_{\rm rad}=0) \equiv 4\pi D_{\rm max}/\lambda P$, the maximum instantaneous Doppler bandwidth when the subradar latitude $\delta_{\rm rad}$ is zero—that is, when the radar has an equatorial view of the target. By comparing this maximum possible bandwidth with the observed bandwidth B, and by recognizing that $B = B_{\rm max}(\delta_{\rm rad}=0)\cos\delta_{\rm rad}$, we can estimate the subradar latitude at the time of radar observations and hence constrain the asteroid's pole direction. These radar-based pole constraints are independent of lightcurve-based pole determinations, except to the (indirect) extent that the latter influence our estimates of the ellipsoid dimensions and hence of $B_{\rm max}(\delta_{\rm rad}=0)$.

In order to estimate ellipsoid dimensions we searched the literature for all relevant data on our target asteroids: lightcurve analyses, radiometry, occultations, speckle interferometry, HST

Table 2
Prior information

Target	Class[a]		D_{IR}[b]	Pole direction[c] (λ, β)	P[d]	Ellipsoid diameters[e]	Refs.[f]	Obs'n year[g]	$\lvert\delta_{rad}\rvert$[h]	$\langle A_{proj}\rangle$[i]	D_{eff}[j]	$B_{max}(\delta_{rad}=0)$[k]
	Tholen	Bus										
3 Juno	S	Sk	234	103, +27	7.2095	321 × 267 × 206 ± 12%	1, 11, 19, 22	2002	36 ± 10	55,300 ± 12,500	265 ± 30	1230 ± 140
7 Iris	S	S	200	20, +10	7.1388	227 × 189 × 189 ± 11%	1	2000	30 ± 10	31,600 ± 6400	201 ± 20	880 ± 93
13 Egeria	G	Ch	208	–	7.045	244 × 218 × 218 ± 16%	–	2001	–	40,500 ± 10,800	227 ± 30	960 ± 150
15 Eunomia	S	S	255	355, −65	6.0827	360 × 257 × 214 ± 11%	2, 12, 13, 14	2002	7 ± 10	52,600 ± 12,100	259 ± 30	1640 ± 190
22 Kalliope	M	X	181	20, −21 or 197, +6	4.1482	204 × 170 × 142 ± 10%	1	2001	23 ± 10	21,900 ± 4600	167 ± 17	1360 ± 140
23 Thalia	S	S	108	359, −55	12.3122	124 × 112 × 86 ± 11%	2	2001	31 ± 15	8900 ± 2000	106 ± 12	278 ± 32
25 Phocaea	S	S	75	–	9.945	107 × 91 × 57 ± 22%	22	2002	–	4400 ± 2000	75 ± 17	299 ± 65
28 Bellona	S	S	121	83, +17 or 275, +40	15.695	140 × 110 × 92 ± 12%	3	2002	18 ± 10	9400 ± 2300	110 ± 13	248 ± 29
31 Euphrosyne	C	Cb	256	115, −30 or 275, −60	5.531	341 × 310 × 194 ± 18%	3, 4	2000	33 ± 20	61,400 ± 18,700	280 ± 43	1710 ± 310
36 Atalante	C	–	106	119, −19	9.93	123 × 96 × 96 ± 12%	5	2001	11 ± 15	8300 ± 1900	103 ± 11	342 ± 40
38 Leda	C	Cgh	116	–	12.84	128 × 110 × 110 ± 16%	–	2001	–	10,600 ± 2300	116 ± 13	276 ± 43
46 Hestia	P	Xc	124	–	21.04	133 × 120 × 120 ± 11%	–	2002	–	12,100 ± 1800	124 ± 9	175 ± 20
50 Virginia	P	Ch	100	–	14.31	109 × 95 × 95 ± 17%	–	2001	–	7800 ± 2000	100 ± 13	212 ± 36
53 Kalypso	PC	–	115	–	17. or 26.56	130 × 108 × 108 ± 18%	–	2002	–	10,500 ± 2500	115 ± 14	212 ± 37 or 136 ± 24
54 Alexandra	C	C	166	160, +45 or 290, +55	7.024	199 × 150 × 150 ± 17%	3	2001	29 ± 20	21,300 ± 4900	165 ± 19	790 ± 130
60 Echo	S	S	60	95, +34 or 275, +42	25.206	67 × 57 × 57 ± 15%	3	2001	22 ± 10	2890 ± 630	60 ± 7	74 ± 11
66 Maja	C	Ch	72	162, −50 or 156, +62	9.733	107 × 64 × 54 ± 14%	5, 9	2001	13 ± 17	3760 ± 980	69 ± 9	304 ± 43
83 Beatrix	M	X	81	4, −42 or 172, −34	10.16	100 × 80 × 73 ± 12%	3	2001	31 ± 10	5500 ± 1200	84 ± 9	272 ± 33
85 Io	FC	B	155	105, −45 or 295, −14	6.8751	175 × 159 × 159 ± 12%	2, 15, 22	1999	5 ± 10	20,800 ± 4900	163 ± 19	704 ± 83
88 Thisbe	CF	B	201	207, +48	6.0413	235 × 214 × 178 ± 11%	2, 11, 22	2000	30 ± 10	33,600 ± 7100	207 ± 22	1080 ± 120
101 Helena	S	S	66	–	23.080	71 × 63 × 63 ± 16%	–	2001	–	3400 ± 770	66 ± 7	86 ± 14
109 Felicitas	GC	Ch	89	–	13.191	93 × 88 × 88 ± 15%	–	2002	–	6300 ± 1300	89 ± 9	195 ± 30
111 Ate	C	Ch	135	–	22.2	143 × 130 × 130 ± 15%	20	2000	–	14,200 ± 3200	135 ± 15	179 ± 27
114 Kassandra	T	Xk	100	–	10.758	116 × 92 × 92 ± 16%	16	2001	–	7800 ± 2200	100 ± 14	298 ± 49
127 Johanna	CX	Ch	–	–	11.	130 × 110 × 110 ± 20%	–	2002	–	10,800 ± 3800	117 ± 21	328 ± 100
128 Nemesis	C	C	188	–	39.	200 × 182 × 182 ± 15%	–	2001	–	27,800 ± 6100	188 ± 21	142 ± 25
137 Meliboea	C	–	145	149, +8	15.13	161 × 136 × 123 ± 14%	9	2002	52 ± 20	16,200 ± 3600	144 ± 16	294 ± 42
145 Adeona	C	Ch	151	–	8.1	159 × 147 × 147 ± 15%	–	2001	–	17,900 ± 4200	151 ± 18	544 ± 82
182 Elsa	S	S	44	–	80.	65 × 34 × 34 ± 27%	–	2002	–	1500 ± 670	44 ± 10	22 ± 6
192 Nausikaa	S	Sl	103	306, −7	13.6225	118 × 91 × 83 ± 10%	1	2000	1 ± 10	6800 ± 1400	93 ± 9	240 ± 24
198 Ampella	S	S	57	–	10.383	65 × 53 × 53 ± 16%	–	1999	–	2570 ± 730	57 ± 8	174 ± 28
211 Isolda	C	Ch	143	–	18.365	151 × 139 × 139 ± 15%	–	2001	–	16,100 ± 3700	143 ± 16	229 ± 34
216 Kleopatra	M	Xe	135	72, +27	5.385	217 × 94 × 81 ± 14%	12, 17, 21, 22	1999	61 ± 10	14,900 ± 4300	138 ± 20	1120 ± 160
225 Henrietta	F	–	120	135, +13	7.356	148 × 119 × 108 ± 16%	3, 6	2001	48 ± 20	12,800 ± 3300	128 ± 16	559 ± 91
247 Eukrate	CP	Xc	134	–	12.10	143 × 130 × 130 ± 15%	–	2001	–	14,200 ± 3200	134 ± 15	328 ± 49
253 Mathilde	C	Cb	58	–	417.7	66 × 48 × 46 ± 5%	18	2001	–	2210 ± 350	53 ± 4	4.37 ± 0.21
266 Aline	C	Ch	109	–	12.3	116 × 106 × 106 ± 18%	–	2001	–	9300 ± 2500	109 ± 15	262 ± 47
270 Anahita	S	*Sl*	51	285, +53	15.06	62 × 50 × 38 ± 20%	10	2001	14 ± 25	1750 ± 530	47 ± 7	114 ± 23
313 Chaldaea	C	–	96	–	8.392 or 10.1	111 × 89 × 89 ± 17%	–	2003	–	7300 ± 2100	96 ± 14	366 ± 61 or 304 ± 51
324 Bamberga	CP	*Cb*	229	–	29.43	239 × 227 × 227 ± 7%	11, 22	2000	–	41,300 ± 4500	229 ± 12	225 ± 15
336 Lacadiera	D	Xk	69	–	13.70	85 × 62 × 62 ± 18%	–	2000	–	3770 ± 970	69 ± 9	171 ± 31

(*continued on next page*)

Table 2 (*continued*)

Target	Class[a]		D_{IR}[b]	Pole direction[c] (λ, β)	P[d]	Ellipsoid diameters[e]	Refs.[f]	Obs'n year[g]	$\lvert\delta_{rad}\rvert$[h]	$\langle A_{proj}\rangle$[i]	D_{eff}[j]	$B_{max}(\delta_{rad}=0)$[k]
	Tholen	Bus										
354 Eleonora	S	Sl	155	356, +20	4.2772	$186 \times 155 \times 141 \pm 11\%$	1	2001	52 ± 10	$21{,}300 \pm 4600$	165 ± 18	1200 ± 130
393 Lampetia	C	Xc	97	–	38.7	$136 \times 120 \times 120 \pm 19\%$	7	2000	–	$12{,}300 \pm 4000$	125 ± 20	98 ± 19
405 Thia	C	Ch	125	–	10.08	$137 \times 119 \times 119 \pm 15\%$	–	2002	–	$12{,}300 \pm 3100$	125 ± 16	376 ± 57
429 Lotis	C	*Xk*	70	–	13.577	$80 \times 64 \times 64 \pm 17\%$	–	2002	–	3800 ± 1100	70 ± 10	164 ± 28
444 Gyptis	C	C	163	–	6.214	$189 \times 164 \times 137 \pm 14\%$	22	2002	–	$20{,}900 \pm 7000$	163 ± 27	842 ± 120
488 Kreusa	C	*Ch*	150	–	19.26	$169 \times 141 \times 141 \pm 16\%$	–	2002	–	$17{,}700 \pm 4900$	150 ± 21	243 ± 39
505 Cava	FC	–	–	138, +40 or 325, +27	8.1789	$126 \times 103 \times 86 \pm 18\%$	8	2001	48 ± 20	8700 ± 2800	105 ± 17	427 ± 78
532 Herculina	S	S	222	289, +10	9.4050	$235 \times 213 \times 178 \pm 11\%$	1, 22	2001	21 ± 10	$32{,}500 \pm 7000$	203 ± 22	692 ± 79
554 Peraga	FC	Ch	96	–	13.63	$115 \times 94 \times 94 \pm 17\%$	22	2000	–	8000 ± 2000	101 ± 13	234 ± 40
622 Esther	S	S	–	–	47.5	$40 \times 24 \times 24 \pm 26\%$	–	2001	–	660 ± 350	29 ± 8	23 ± 6
654 Zelinda	C	Ch	127	–	31.9	$151 \times 116 \times 116 \pm 18\%$	–	2002	–	$12{,}700 \pm 3600$	127 ± 18	131 ± 23
704 Interamnia	F	B	317	45, −12 or 226, −10	8.727	$343 \times 298 \times 278 \pm 12\%$	3, 22	2001	50 ± 20	$76{,}200 \pm 16{,}400$	312 ± 33	1090 ± 130
914 Palisana	CU	*Ch*	77	–	15.62	$85 \times 72 \times 72 \pm 16\%$	16	2000	–	4600 ± 1200	77 ± 10	151 ± 25
1963 Bezovec	C	–	45	–	18.160	$63 \times 36 \times 36 \pm 23\%$	–	2001	–	1570 ± 650	45 ± 9	96 ± 23

[a] Taxonomic classification on the Tholen system (Tholen, 1989) and the Bus system (Bus and Binzel, 2002a, 2002b) based on visual and infrared data. Based on their visual albedos (Tedesco et al., 2002) 50 Virginia, 53 Kalypso, and 83 Beatrix were reassigned from Tholen classes X, XC, and X to P, PC, and M, respectively; no visual albedo estimate is available for 127 Johanna (Tholen class CX). Tholen class for 253 Mathilde taken from Binzel et al. (1996) and Rivkin et al. (1997). Bus classes are listed in italics for five asteroids that were not classified by Bus and Binzel (2002a, 2002b) but were classified on the Bus system by Lazzaro et al. (2004).

[b] Radiometric diameter (km) based on IRAS data (Tedesco et al., 2002).

[c] Ecliptic longitude and latitude (deg) of the spin vector; see footnote f for references.

[d] Sidereal rotation period (h). Most values were taken from the compilation by Harris (2005); see footnote f for additional references.

[e] Adopted axis dimensions (km) based on a combination of all available radiometric, lightcurve, occultation, and imaging data (see text). The stated percentage standard error refers to the largest diameter $2a$. Radiometry was taken primarily from IRAS data (Tedesco et al., 2002), with TRIAD results (Bowell et al., 1979) sometimes considered as well. Maximum lightcurve amplitudes used to estimate some axis ratios were taken from Harris (2005), as were taxonomy-based assumed visual albedos used to estimate diameters for 127 Johanna, 505 Cava, and 622 Esther. See footnote f for additional references.

[f] Additional references used to obtain estimates listed in the preceding three columns: (1) Kaasalainen et al. (2002a); (2) Torppa et al. (2003); (3) Magnusson (1995); (4) Kryszczyńska et al. (1996); (5) Blanco and Riccioli (1998); (6) Michałowski et al. (2000); (7) Holliday (2001); (8) Michałowski (1996); (9) Blanco et al. (2000); (10) Tungalag et al. (2002); (11) Cellino et al. (2003); (12) Tanga et al. (2003); (13) Hestroffer et al. (2002b); (14) Ragazzoni et al. (2000); (15) Erikson et al. (1999); (16) Dotto et al. (2002); (17) Ostro et al. (2000); (18) Veverka et al. (1997); (19) Shinokawa et al. (2002); (20) Brown and Morrison (1984); (21) Hestroffer et al. (2002a); (22) Millis and Dunham (1989); Dunham et al. (2002); Dunham (2003), and references therein. Frequently used references not explicitly listed here are Harris (2005), Tedesco et al. (2002), and Bowell et al. (1979) (see footnotes d and e).

[g] Year of radar observation.

[h] Absolute value of the subradar latitude (deg) over the duration of radar observations, based on photometric pole estimates (see footnote c).

[i] Mean projected area (km^2) of the reference ellipsoid as viewed by the radar. This is an unweighted mean over all rotation phases. The stated standard error incorporates uncertainties in the axis lengths, differences between the radar viewing geometry and the viewing geometry for radiometric (or occultation or imaging) measurements, and the rotation phase coverage for radar and radiometric data.

[j] Effective diameter (km) of the target. By definition, the mean projected area of the reference ellipsoid as viewed by the radar is equal to $\pi D_{eff}^2/4$. Standard errors propagate from those stated for $\langle A_{proj}\rangle$.

[k] Maximum-breadth echo bandwidth (Hz) predicted by the reference ellipsoid for a spectral sum obtained with an equatorial view and complete rotation phase coverage. Standard errors propagate from those stated for diameter $2a$.

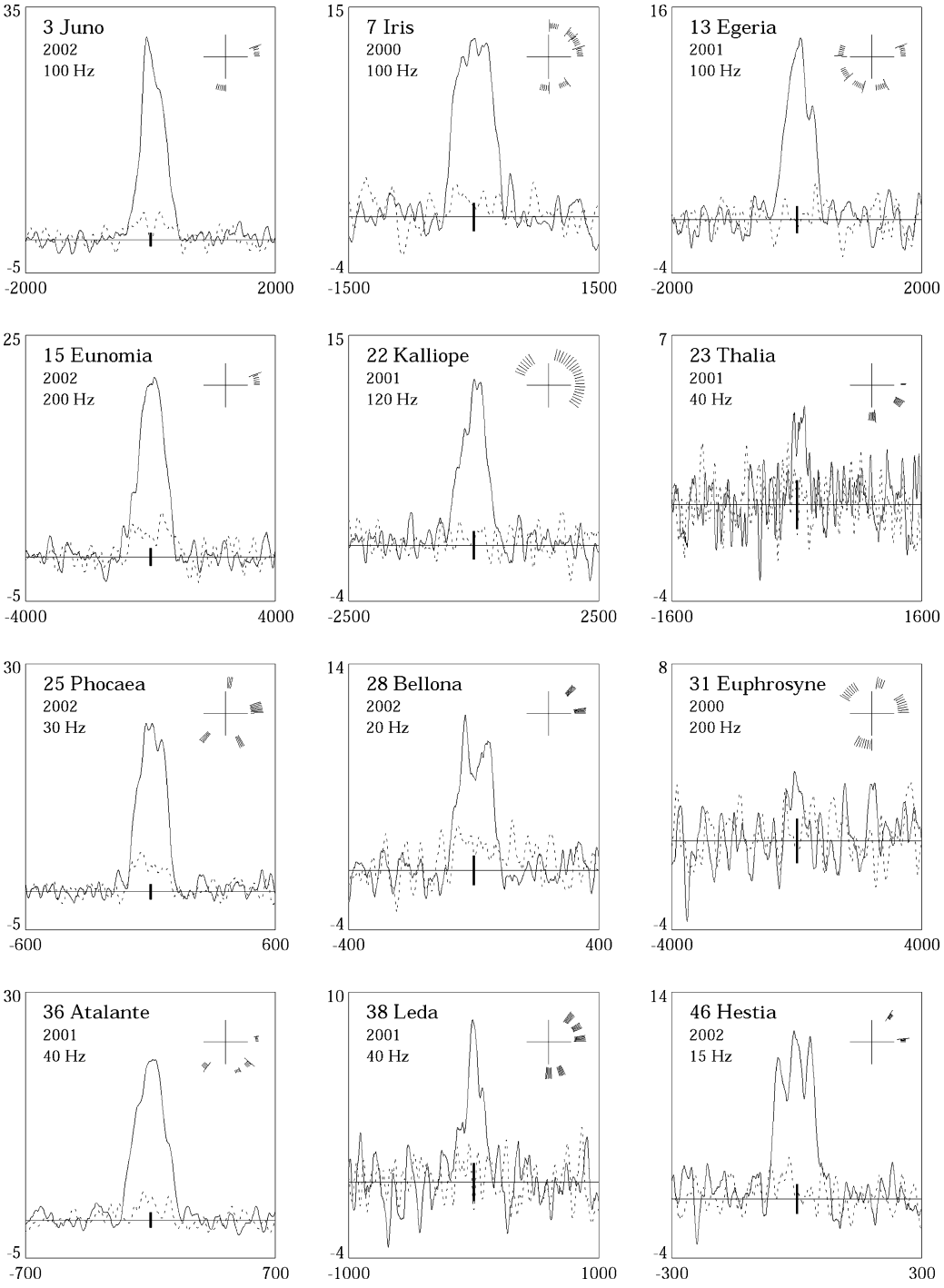

Fig. 1. Weighted sums of OC (solid lines) and SC (dashed lines) echo spectra for all 55 radar experiments. Echo power, in units of standard deviations of the noise, is plotted versus Doppler frequency (Hz) relative to that of hypothetical echoes from the target's center of mass. The vertical bar at the origin indicates ±1 standard deviation of the OC noise. Each label gives the target name, the observation year, and the frequency resolution of the displayed data. Rotation phase coverage is depicted in the upper right portion of each plot. Each radial line segment denotes the phase (relative to an arbitrary epoch) of an independent spectrum formed by summing a 4-min data "block" (see Section 2); the length of the segment is proportional to the OC noise standard deviation of the corresponding spectrum. The last block in a run is typically shorter than 4 min, resulting in a longer line segment.

data, etc. For each object, we studied the available information and decided on a consensus model ellipsoid.

Selected asteroid properties taken from the literature, and the resulting estimates of reference ellipsoid dimensions, $\langle A_{\rm proj}\rangle$, and $B_{\rm max}(\delta_{\rm rad}=0)$, are listed in Table 2. The pole estimates given in this table, and the corresponding a priori subradar latitude predictions, are *not* the radar-based estimates described earlier but are derived instead from lightcurve analyses and other literature data. (Radar-based pole results will be discussed later.)

We now turn to the radar spectra. Summing spectral values over the signal range yields radar cross sections $\sigma_{\rm OC}$ and $\sigma_{\rm SC}$,

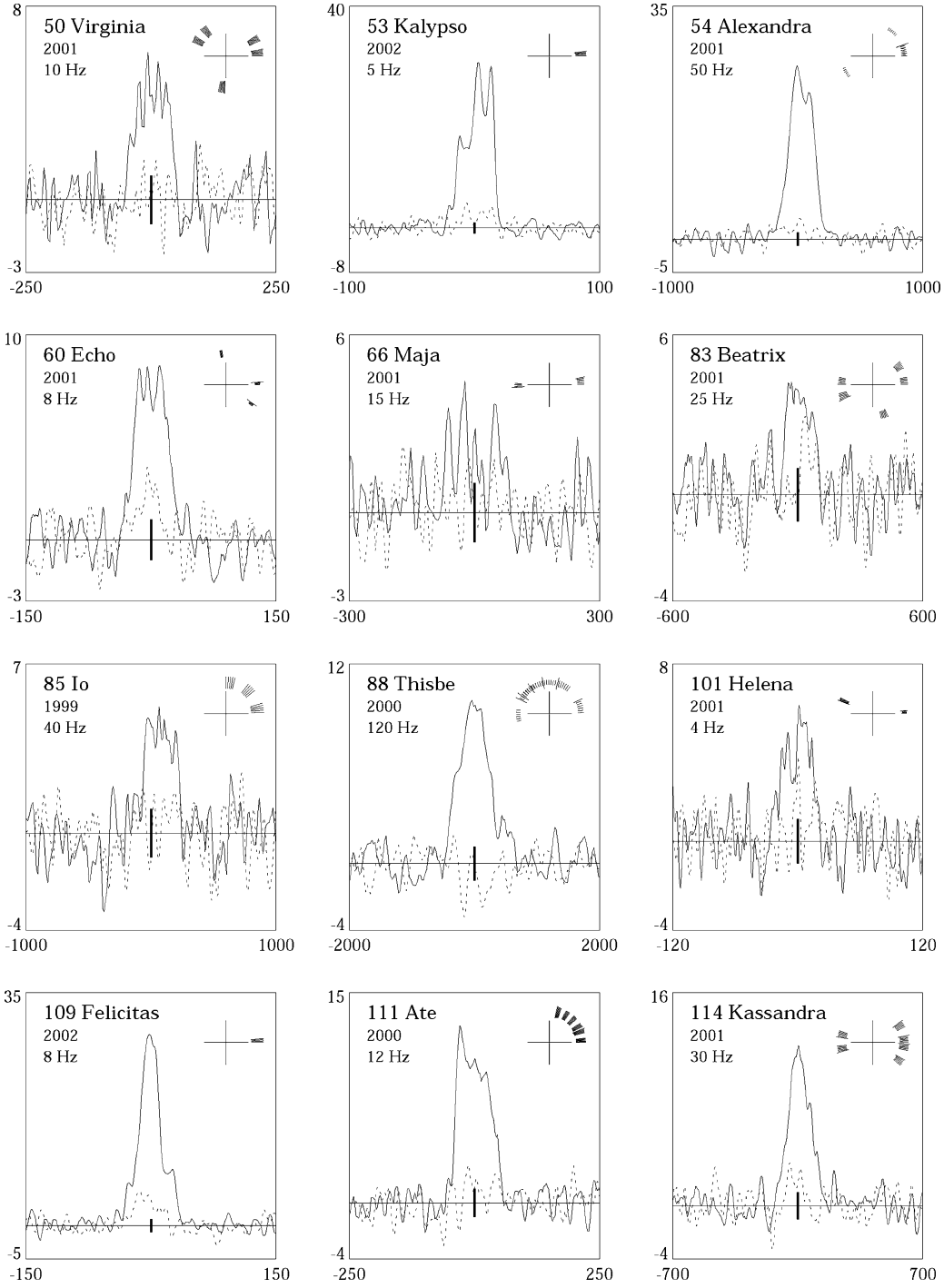

Fig. 1. (*continued*)

and from these two parameters we can estimate circular polarization ratio $\mu_C \equiv \sigma_{SC}/\sigma_{OC}$. Dividing OC cross section by $\langle A_{proj} \rangle$ gives us OC albedo $\hat{\sigma}_{OC}$, our zeroth-order measure of radar reflectivity.

For most of our targets our $\langle A_{proj} \rangle$ estimates rely strongly on radiometric IRAS diameters (see Table 2), for which systematic error is thought to be less than 10% (Tedesco et al., 2002). This implies that systematic error on our $\langle A_{proj} \rangle$ and $\hat{\sigma}_{OC}$ estimates should be better than 20%. Such biases would have no effect on our statistical analyses unless there were different biases for different taxonomic classes. While we cannot rule out taxonomy-dependent diameter biases—which might result from different mineralogies, or from different surface temperatures (due to different mean heliocentric distances)—we also cannot place any useful constraints on them at present.

For ten targets we have both CW spectra and delay-Doppler images obtained within a few days of each other; the images will be fully analyzed and discussed elsewhere, but here we use them to derive disk-integrated properties σ_{OC} and μ_C so that we can compare the results to CW-based estimates. These two sets

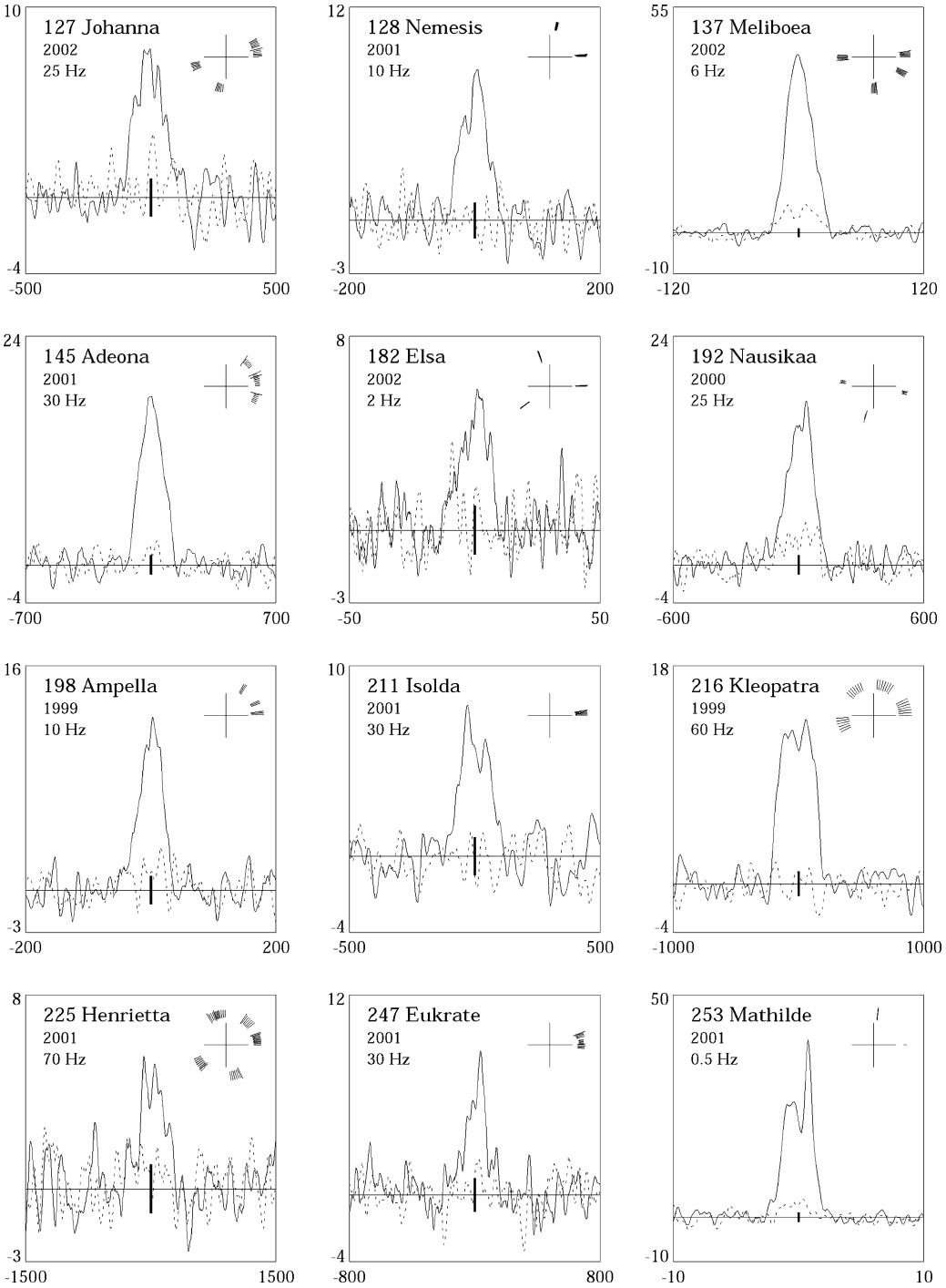

Fig. 1. (*continued*)

of cross sections and polarization ratios, and our adopted best estimates for each target, are given in Table 3; details on how we combined the two sets are given in a footnote to the table.

As mentioned earlier, measuring Doppler bandwidth B for a spectral sum allows us to constrain an asteroid's pole direction; however it is usually much more difficult (and subjective) to obtain B than to estimate σ_{OC} or μ_{C}. Ideally we use the spectral sum's zero-crossing bandwidth B_{ZC} as our estimator for B, but this requires smoothing the spectrum in frequency and folding it about zero Doppler, and still is very sensitive to the presence of baseline noise. (We fold the spectrum not only to increase SNR but also to compensate for incomplete rotation phase coverage: the nulls [zero crossings] of a noise-free spectral sum with complete rotation phase coverage should be symmetric about zero Doppler.) A more robust parameter, which provides a conservative lower limit to B in cases where no credible estimate of B_{ZC} is possible, is equivalent bandwidth B_{eq}, defined as

$$B_{\mathrm{eq}} = \frac{(\sum_i S_i)^2}{\sum_i (S_i)^2}\Delta f, \tag{2}$$

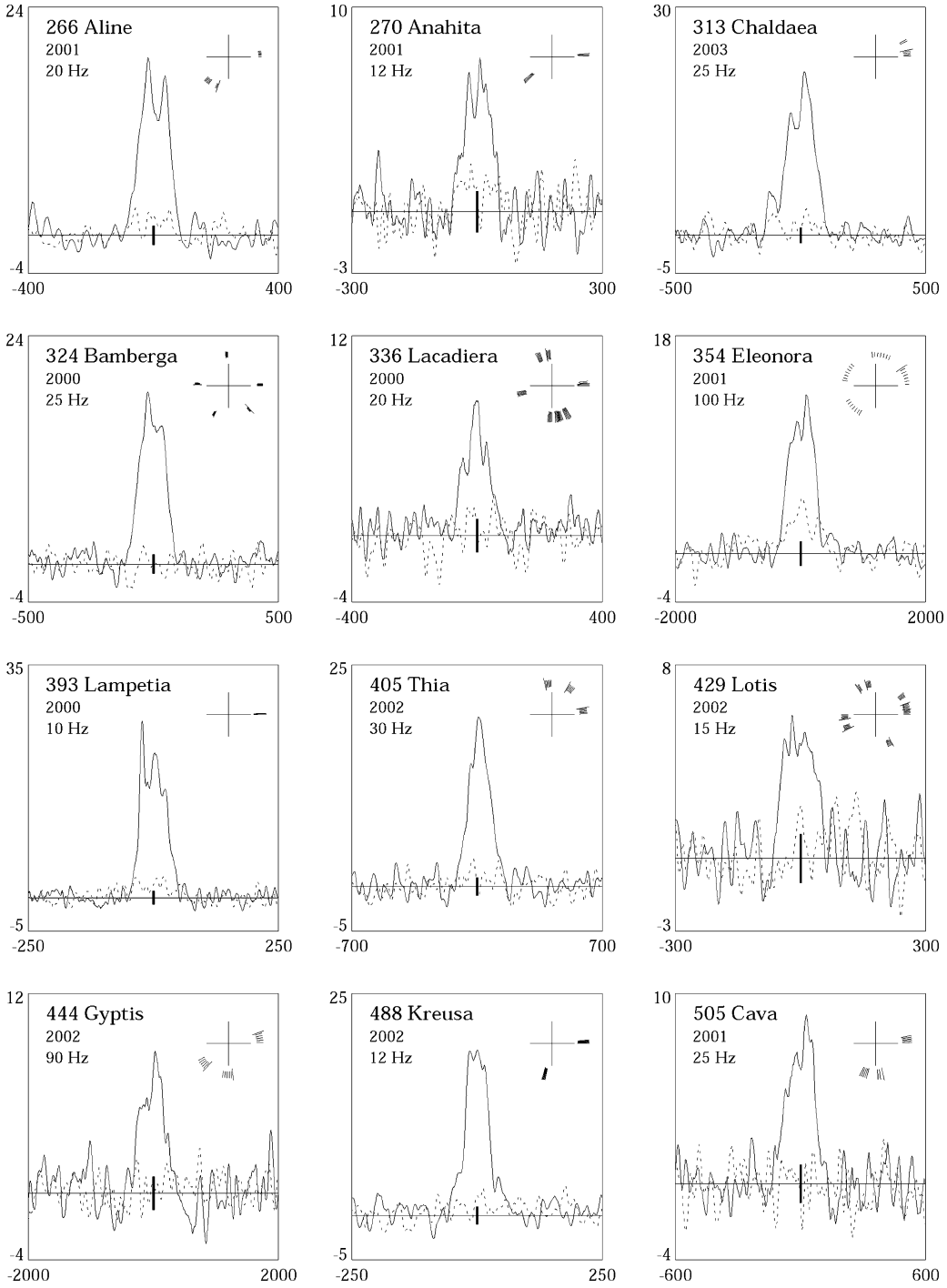

Fig. 1. (*continued*)

where S_i is the signal in the ith frequency channel, and the sums are taken over all channels that contain echo power (Tiuri, 1964). Estimating $B_{\rm eq}$ does not involve folding and requires much less smoothing than is needed for estimating $B_{\rm ZC}$. The estimate will be biased low if the signal range is chosen incorrectly—that is, if the sums in Eq. (2) are carried out over too few or too many frequency channels. However, in practice this bias will generally be small. Visual inspection of the spectrum will protect us from choosing much too narrow a signal range. It is conceivable that for a weak signal whose "tails" are lost in the noise we could choose much too large a signal range: the noise contribution to the denominator of Eq. (2) might then be comparable to the signal contribution, significantly lowering $B_{\rm eq}$. Even in this extreme case, the biased $B_{\rm eq}$ estimate would still serve as a valid lower limit on B.

Table 4 lists the parameters estimated from our radar spectra for each of the 55 experiments reported here, along with the corresponding pole constraints. The most striking feature of Table 4 is that all but one of the 55 targets was detected at the six-sigma level or better, despite the fact that their mean

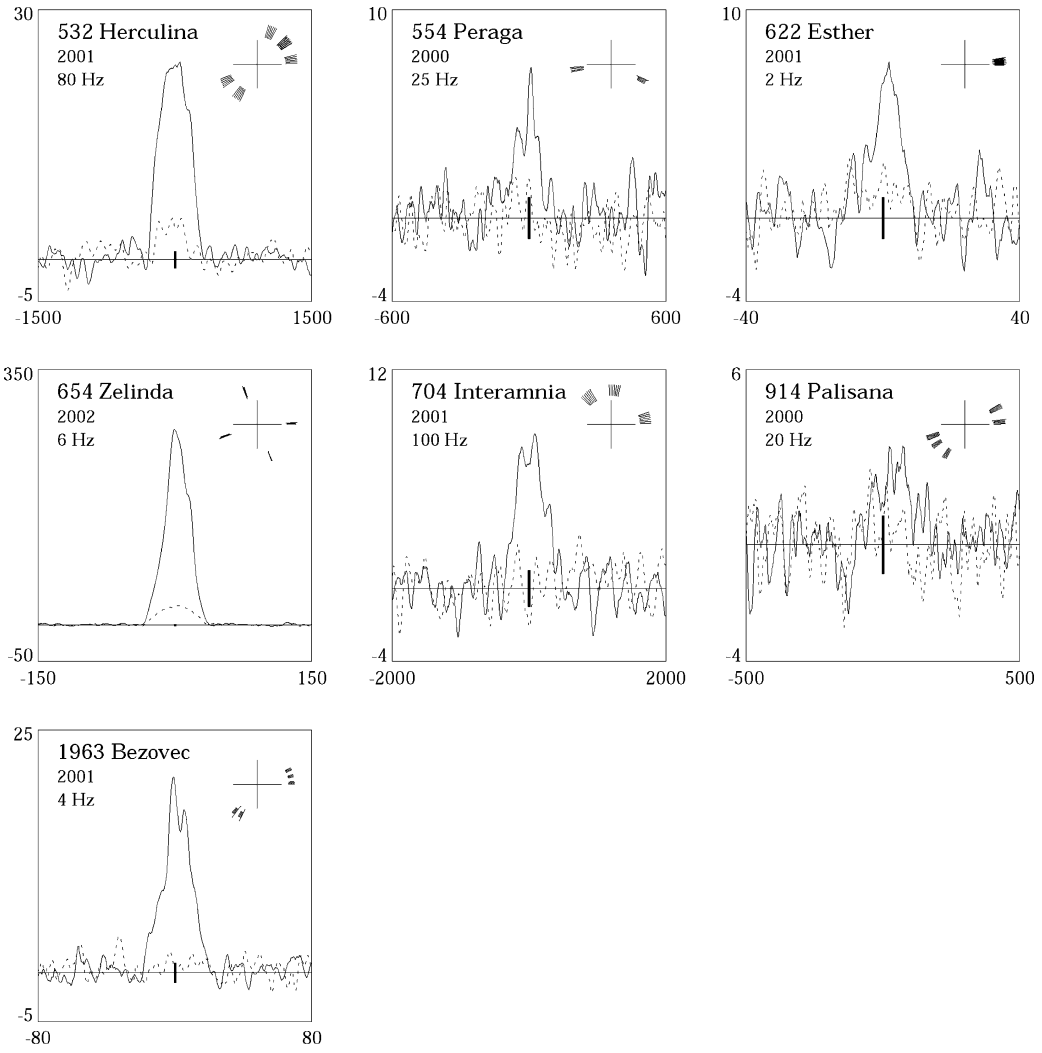

Fig. 1. (*continued*)

Table 3
Disk-integrated properties: CW spectra vs delay-Doppler images

Target	Year	Runs		μ_C		σ_{OC} (km^2)		
		CW	Images	CW = adopted	Images	CW	Images	Adopted
15 Eunomia	2002	1	17	0.17 ± 0.03	0.16	6230	4460	4460 ± 1150
25 Phocaea	2002	4	20	0.18 ± 0.03	0.33	460	390	440 ± 130
53 Kalypso	2002	1	4	0.12 ± 0.02	0.12	2070	2190	2110 ± 530
109 Felicitas	2002	1	10	0.13 ± 0.03	0.10	490	590	590 ± 150
192 Nausikaa	2000	3	16	0.22 ± 0.04	0.38	890	590	790 ± 250
253 Mathilde	2001	3	15	0.08 ± 0.02	0.12	156	167	160 ± 40
324 Bamberga	2000	5	10	0.00 ± 0.04	0.00	1280	1350	1280 ± 330
393 Lampetia	2000	1	5	0.14 ± 0.03	0.11	1430	880	1250 ± 400
554 Peraga	2000	2	12	0.00 ± 0.13	–	1650	800	1500 ± 750
654 Zelinda	2002	4	30	0.13 ± 0.01	0.11	2590	2720	2590 ± 660

Note. Polarization ratios estimated from delay-Doppler images are shown for comparison purposes only, as they are far more uncertain than the corresponding ratios estimated from CW spectra. Images of 554 Peraga were too weak for us to estimate μ_C. The relative weight given to OC cross section estimates from CW spectra and from images was subjectively determined based on the degree to which images improve rotation phase coverage and on the reliability of the imaging system, with the latter generally best for the five imaging experiments from 2002. For 25 Phocaea, 53 Kalypso, 192 Nausikaa, 253 Mathilde, and 393 Lampetia we give double-weight to CW-based estimates, since images are inherently noisier than CW spectra. For 324 Bamberga and 654 Zelinda the images do not significantly improve rotation phase coverage and so we adopt the CW-based estimates. We adopt the image-based estimates for 15 Eunomia and 109 Felicitas, since in both cases the single CW-based estimate agrees well with cross sections derived from images taken at similar rotation phase. The two individual CW runs for Peraga yield σ_{OC} estimates of 2500 and 1300 km^2, discrepant with each other and with the image-based estimate of 800 km^2; hence we take the unweighted mean of these three values as our best estimate and assign a conservative 50% standard error. See footnotes to Table 4 for discussion of the standard errors listed for polarization ratios and cross sections.

Table 4
Radar properties by experiment

Target	Year[a]	OC SNR[b]	B_{eq} (Hz)[c]	B_{ZC} (Hz)[d]	μ_C[e]	σ_{OC} (km^2)[f]	D_{eff} (km)[g]	$\hat{\sigma}_{OC}$[h]	$\lvert\delta_{rad}\rvert$ (°)[i]	λ, β (°)[j]
3 Juno	2002	52	585 ± 10	980 ± 200	0.16 ± 0.03	7500 ± 1900	265 ± 30	0.14 ± 0.05	0−63	143, −11
7 Iris	2000	26	570 ± 30	$\geqslant 600$	0.11 ± 0.04	5600 ± 1400	201 ± 20	0.18 ± 0.06	0−56	139, −7
13 Egeria	2001	24	630 ± 30	850 ± 150	0.06 ± 0.05	2400 ± 610	227 ± 30	0.059 ± 0.023	0−58	187, +17
15 Eunomia	2002	39	1200 ± 30	$\geqslant 1300$	0.17 ± 0.03	4460 ± 1150	259 ± 30	0.085 ± 0.030	0−50	349, +18
22 Kalliope	2001	22	790 ± 40	1150 ± 300	0.07 ± 0.10	3290 ± 890	167 ± 17	0.15 ± 0.05	0−67	82, +7
23 Thalia	2001	7	210 ± 30	–	0.19 ± 0.11	1310 ± 360	106 ± 12	0.15 ± 0.06	0−58	44, −9
25 Phocaea	2002	44	185 ± 4	260 ± 60	0.18 ± 0.03	440 ± 130	75 ± 17	0.10 ± 0.07	0−65	268, +41
28 Bellona	2002	19	115 ± 6	175 ± 10	0.32 ± 0.06	1020 ± 260	110 ± 13	0.11 ± 0.04	20−56	156, +1
31 Euphrosyne	2000	4	–	–	–	1670 ± 560	280 ± 43	(0.027 ± 0.013)	–	67, +12
36 Atalante	2001	40	260 ± 5	330 ± 20	0.11 ± 0.03	910 ± 230	103 ± 11	0.11 ± 0.04	0−41	48, +19
38 Leda	2001	13	260 ± 20	–	0.09 ± 0.08	800 ± 210	116 ± 13	0.075 ± 0.027	0−48	87, +4
46 Hestia	2002	23	105 ± 5	–	0.10 ± 0.04	780 ± 200	124 ± 9	0.064 ± 0.019	0−62	42, −3
50 Virginia	2001	12	68 ± 4	110 ± 10	0.00 ± 0.08	660 ± 170	100 ± 13	0.085 ± 0.032	36−69	124, −4
53 Kalypso	2002	52	30 ± 2	46 ± 5	0.12 ± 0.02	2110 ± 530	115 ± 14	0.20 ± 0.07	70−82[k] or 57−77	171, +2
54 Alexandra	2001	47	305 ± 10	450 ± 50	0.08 ± 0.03	3200 ± 820	165 ± 19	0.15 ± 0.05	27−67	349, +14
60 Echo	2001	17	50 ± 4	$\geqslant 50$	0.17 ± 0.06	340 ± 90	60 ± 7	0.12 ± 0.04	0−59	34, −2
66 Maja	2001	6	$\geqslant 60$	–	0.22 ± 0.12	310 ± 90	69 ± 9	0.082 ± 0.034	0−81	45, +4
83 Beatrix	2001	9	140 ± 20	–	0.23 ± 0.11	400 ± 110	84 ± 9	0.073 ± 0.026	0−69	129, +8
85 Io	1999	11	225 ± 25	–	0.00 ± 0.12	2020 ± 570	163 ± 19	0.097 ± 0.037	0−77	17, +6
88 Thisbe	2000	18	825 ± 25	$\geqslant 1000$	0.00 ± 0.07	2730 ± 720	207 ± 22	0.081 ± 0.028	0−41	4, +9
101 Helena	2001	12	22 ± 3	50 ± 5	0.32 ± 0.09	260 ± 70	66 ± 7	0.076 ± 0.028	26−66	12, +9
109 Felicitas	2002	46	47 ± 1	$\geqslant 65$	0.13 ± 0.03	590 ± 150	89 ± 9	0.094 ± 0.032	0−75	49, +13
111 Ate	2000	25	85 ± 5	115 ± 15	0.04 ± 0.05	2270 ± 580	135 ± 15	0.16 ± 0.06	11−65	11, +7
114 Kassandra	2001	22	200 ± 10	–	0.11 ± 0.06	900 ± 230	100 ± 14	0.12 ± 0.05	0−61	170, +2
127 Johanna	2002	15	170 ± 10	$\geqslant 190$	0.18 ± 0.07	1140 ± 300	117 ± 21	0.11 ± 0.05	0−69	135, +13
128 Nemesis	2001	15	60 ± 4	90 ± 15	0.00 ± 0.07	1410 ± 370	188 ± 21	0.051 ± 0.018	0−67	98, +5
137 Meliboea	2002	82	39 ± 1	60 ± 5	0.14 ± 0.01	3420 ± 860	144 ± 16	0.21 ± 0.07	73−81	4, +7
145 Adeona	2001	34	206 ± 10	275 ± 30	0.03 ± 0.04	2130 ± 540	151 ± 18	0.12 ± 0.04	41−69	185, +20
182 Elsa	2002	11	12 ± 2	$\geqslant 16$	0.11 ± 0.09	190 ± 50	44 ± 10	0.13 ± 0.08	0−62	161, +2
192 Nausikaa	2000	33	195 ± 6	$\geqslant 220$	0.22 ± 0.04	790 ± 250	93 ± 9	0.12 ± 0.05	0−40	34, +10
198 Ampella	1999	21	60 ± 4	$\geqslant 70$	0.22 ± 0.07	660 ± 170	57 ± 8	0.26 ± 0.11	0−72	345, +19
211 Isolda	2001	13	175 ± 15	$\geqslant 175$	0.00 ± 0.07	2350 ± 620	143 ± 16	0.15 ± 0.05	0−54	44, +2
216 Kleopatra	1999	28	345 ± 10	445 ± 10	0.00 ± 0.05	$10{,}200 \pm 2600$	138 ± 20	0.68 ± 0.28	56−72	64, −1
225 Henrietta	2001	9	400 ± 40	–	0.26 ± 0.11	670 ± 180	128 ± 16	0.052 ± 0.021	0−61	334, +25
247 Eukrate	2001	13	215 ± 15	–	0.10 ± 0.07	550 ± 140	134 ± 15	0.039 ± 0.014	0−62	27, +17
253 Mathilde	2001	60	3.1 ± 0.1	$\geqslant 4.0$	0.08 ± 0.02	160 ± 40	53 ± 4	0.072 ± 0.022	0−33[l]	354, +5
266 Aline	2001	34	131 ± 10	190 ± 20	0.09 ± 0.04	1960 ± 490	109 ± 15	0.21 ± 0.08	0−61	30, +12
270 Anahita	2001	14	80 ± 4	110 ± 10	0.26 ± 0.07	160 ± 40	47 ± 7	0.091 ± 0.039	0−49	359, +5
313 Chaldaea	2003	37	170 ± 4	$\geqslant 180$	0.10 ± 0.03	1080 ± 270	96 ± 14	0.15 ± 0.06	0−68[m] or 0−64	166, 0
324 Bamberga	2000	32	140 ± 4	$\geqslant 170$	0.00 ± 0.04	1280 ± 330	229 ± 12	0.031 ± 0.009	0−48	54, +15
336 Lacadiera	2000	13	112 ± 6	$\geqslant 130$	0.16 ± 0.08	400 ± 110	69 ± 9	0.11 ± 0.04	0−56	349, +10

(*continued on next page*)

Table 4 (*continued*)

Target	Year[a]	OC SNR[b]	B_{eq} (Hz)[c]	B_{ZC} (Hz)[d]	μ_C[e]	σ_{OC} (km^2)[f]	D_{eff} (km)[g]	$\hat{\sigma}_{OC}$[h]	$\lvert\delta_{rad}\rvert$ (°)[i]	λ, β (°)[j]
354 Eleonora	2001	23	600 ± 25	$\geqslant 625$	0.32 ± 0.13	3280 ± 920	165 ± 18	0.15 ± 0.06	0–65	166, +17
393 Lampetia	2000	46	70 ± 2	$\geqslant 85$	0.14 ± 0.03	1250 ± 400	125 ± 20	0.10 ± 0.05	0–51	341, +25
405 Thia	2002	33	178 ± 5	310 ± 40	0.10 ± 0.03	1790 ± 450	125 ± 16	0.15 ± 0.06	0–56	127, −17
429 Lotis	2002	12	95 ± 8	$\geqslant 110$	0.10 ± 0.07	250 ± 70	70 ± 10	0.066 ± 0.028	0–60	15, +8
444 Gyptis	2002	14	540 ± 30	750 ± 150	0.09 ± 0.07	1180 ± 310	163 ± 27	0.056 ± 0.026	0–60	11, +2
488 Kreusa	2002	35	76 ± 2	$\geqslant 90$	0.14 ± 0.13	2610 ± 670	150 ± 21	0.15 ± 0.06	0–74	147, +16
505 Cava	2001	17	165 ± 10	270 ± 50	0.00 ± 0.07	570 ± 150	105 ± 17	0.066 ± 0.030	0–69	114, +7
532 Herculina	2001	48	490 ± 10	590 ± 20	0.15 ± 0.03	3230 ± 840	203 ± 22	0.099 ± 0.035	0–47	217, +27
554 Peraga	2000	7	180 ± 30	–	0.00 ± 0.13	1500 ± 750	101 ± 13	0.19 ± 0.11	0–61	92, +2
622 Esther	2001	13	12 ± 1	$\geqslant 14$	0.35 ± 0.09	77 ± 20	29 ± 8	0.12 ± 0.09	0–66	98, −10
654 Zelinda	2002	510	45 ± 2	76 ± 6	0.13 ± 0.01	2590 ± 660	127 ± 18	0.20 ± 0.08	24–66	104, −15
704 Interamnia	2001	15	600 ± 40	740 ± 50	0.04 ± 0.08	4500 ± 1200	312 ± 33	0.059 ± 0.021	24–58	18, +27
914 Palisana	2000	6	100 ± 20	–	0.44 ± 0.16	290 ± 80	77 ± 10	0.063 ± 0.025	0–67	347, +46
1963 Bezovec	2001	33	25 ± 1	36 ± 5	0.06 ± 0.04	190 ± 50	45 ± 9	0.12 ± 0.07	42–77	83, −8

[a] Year of radar observation.

[b] The OC SNR is the signal-to-noise ratio for an optimally filtered, weighted sum of all OC echo spectra.

[c] By definition (Tiuri, 1964), equivalent bandwidth $B_{eq} = \Delta f[(\sum S_i)^2 / \sum S_i^2]$, where S_i are the OC spectral elements and Δf is the "raw" frequency resolution. Wishing to smooth in frequency just enough to minimize the influence of random baseline noise on our estimate, we take unfolded spectra and compute B_{eq} for several frequency resolutions. These values sometimes exhibit large fluctuations at fine resolutions, but they become more stable, and increase slowly and steadily at coarser resolutions. In such cases, stated estimates B_{eq} refer to a resolution at the boundary between these two regimes; otherwise we use the raw resolution to obtain B_{eq}. Uncertainties are subjectively determined by inspecting the fluctuations in B_{eq} near the chosen resolution.

[d] B_{ZC} is the zero-crossing bandwidth of the weighted sum of all OC spectra, folded about zero Doppler and smoothed in frequency. The degree of smoothing is determined as described above for B_{eq}; coarser effective resolution is usually required for obtaining B_{ZC} than for obtaining B_{eq}. Uncertainties are subjectively determined by inspecting the fluctuations in the zero-crossing bandwidth near the chosen resolution.

[e] μ_C is the circular polarization ratio, SC/OC. Standard errors quoted for μ_C are obtained by first determining, for both the SC and the OC spectrum, the standard deviation of the receiver noise in the OC equivalent bandwidth (B_{eq}). In order to account for baseline uncertainty, this receiver-noise cross section for each polarization channel is added in quadrature to the signal contained in a rectangular box that is as wide as the signal limits and is F noise standard deviations high; F is set equal to the r.m.s. offset removed via explicit baseline subtraction (see Section 2) performed on the various runs for this target, or else 0.05, whichever is larger. The resulting random uncertainties on the SC and OC cross sections are used to find the error on μ_C (Ostro et al., 1983).

[f] σ_{OC} is the OC radar cross section. Assigned standard errors are the root sum square of the random uncertainty (see footnote e) and the systematic calibration error; the latter is estimated as 25% of σ_{OC}, and is generally much larger than the random uncertainty.

[g] D_{eff} is the effective diameter of the target. By definition, the mean projected area of the reference ellipsoid as viewed by the radar is equal to $\pi D_{eff}^2/4$. The stated standard error incorporates uncertainties in the axis lengths, differences between the radar viewing geometry and the viewing geometry for radiometric (or occultation or imaging) measurements, and the rotation phase coverage for radar and radiometric data.

[h] The OC radar albedo, $\hat{\sigma}_{OC}$, is equal to $\sigma_{OC}/(\pi D_{eff}^2/4)$. Standard errors propagate from those given for σ_{OC} and D_{eff} (Ostro et al., 1983). Error intervals for ratios are in fact asymmetric, with the positive error greater than the negative, particularly when the denominator (here the mean projected area viewed by the radar) has a large fractional uncertainty; for simplicity we instead quote a symmetric one-sigma error interval obtained by taking the mean of the positive and negative formal errors.

[i] Absolute value of the subradar latitude over the duration of radar observations, computed as $\lvert\delta_{rad}\rvert = \cos^{-1}[B/B_{max}(\delta_{rad} = 0)]$. All stated ranges are at the 95% confidence level.

[j] Ecliptic longitude and latitude at the weighted midpoint of radar observations.

[k] Top and bottom entries for 53 Kalypso refer to $P = 17$ h and $P = 26.56$ h, respectively.

[l] If 253 Mathilde is in a non-principal-axis rotation state as suggested by Mottola et al. (1995) then the listed pole constraint is not meaningful.

[m] Top and bottom entries for 313 Chaldaea refer to $P = 8.392$ h and $P = 10.1$ h, respectively.

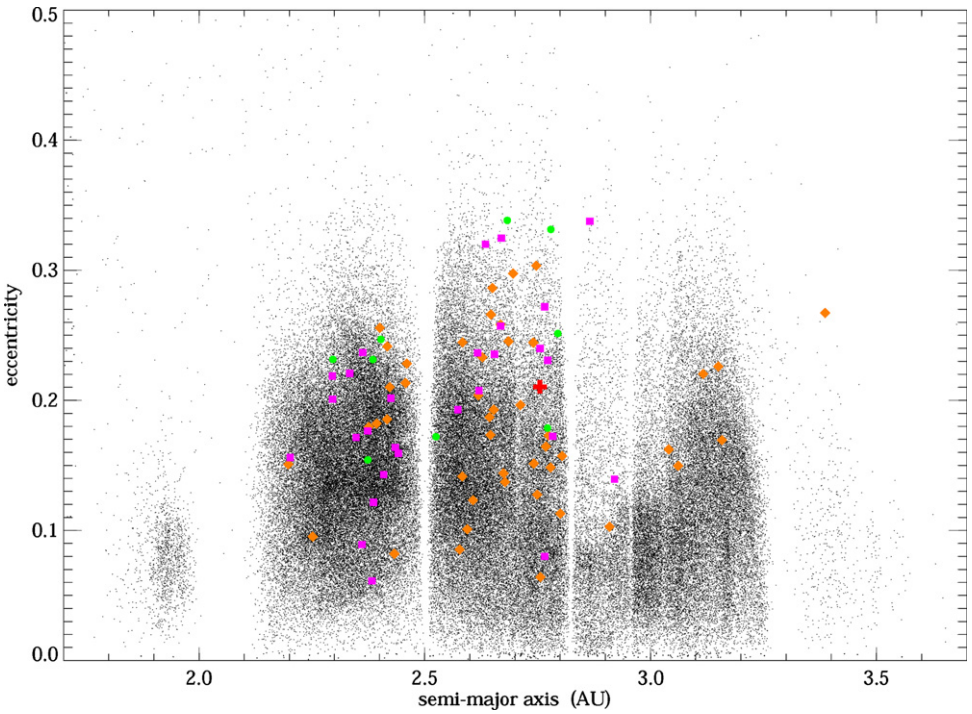

Fig. 2. Eccentricity vs semimajor axis for radar targets and other main-belt asteroids. Orbital elements for 129,436 numbered asteroids (available at http://ssd.jpl.nasa.gov) are plotted as black dots. Orange diamonds denote the 46 post-upgrade radar targets from Table 4 that were not discussed in Paper I; magenta squares denote the 28 pre-upgrade targets from Paper I that are not in Table 4; green circles denote the nine targets (7 Iris, 46 Hestia, 192 Nausikaa, 216 Kleopatra, 324 Bamberga, 393 Lampetia, 532 Herculina, 554 Peraga, and 654 Zelinda) that are in both Table 4 and Paper I; and the red cross denotes 288 Glauke, a post-upgrade target (Ostro et al., 2001) that is not in Table 4.

distance from Earth was 1.33 AU, 11% greater than the mean distance to the 37 MBAs discussed in Paper I. (If we throw out the unusually large pre-upgrade targets 1 Ceres, 2 Pallas, and 4 Vesta, the post-upgrade targets are about 20% further away in the mean.) Thus, as expected, the Arecibo upgrade has enabled us to probe further out into the main belt while maintaining a nearly 100% detection rate.

We make a similar point graphically in Fig. 2, a plot of eccentricity e vs semi-major axis a for over 129,000 numbered asteroids, with special plotting symbols used for our pre-upgrade and post-upgrade radar targets. The 55 targets reported here have a larger mean semi-major axis than do the 37 pre-upgrade targets (2.66 AU vs 2.54 AU) and a slightly lower mean eccentricity (0.19 vs 0.21). (Nine MBAs are common to both samples.) Apart from a bias against low-eccentricity objects in the outer main belt, the radar-observed MBAs represent a reasonable sampling of the most populated region of the belt in (a, e) space.

The radar-based pole constraints (i.e., constraints on the value of $|\delta_{\rm rad}|$ at the time of observation) listed in Table 4 range from very loose to very restrictive. For a given target, if the zero-crossing bandwidth $B_{\rm ZC}$ is highly uncertain, or if we can only place a lower limit on the bandwidth ($B \geqslant B_{\rm eq}$) and that lower limit is very low, the resulting subradar latitude error interval is extremely wide. (The table lists 95% error intervals for subradar latitude, not one-sigma intervals.) Thus for the very weak target 66 Maja we find that $|\delta_{\rm rad}|$ could have been anywhere between 0° and 81°. As a result, we can only say that this asteroid's pole direction is *not* located within two 9-degree-radius circles on the sky, one centered at Maja's sky position during the radar observations and one centered at the antipodal position. At the other extreme, the strong, narrow signal received from 137 Meliboea tells us that we had a nearly pole-on view of this asteroid, restricting the pole direction to a pair of small, narrow annuli (inner radius 9°, outer radius 17°) centered on opposite sides of the sky. This radar-based constraint is roughly consistent with, but far more stringent than, the a priori subradar latitude prediction obtained from Meliboea's lightcurve-based pole estimate (see Table 2).

By combining the new results in Table 4 with the pre-upgrade radar data summarized in Paper I and with two post-upgrade experiments described by Ostro et al. (2000, 2001) we obtain a total of 83 detections of 84 observed MBAs. The mean radar properties of these targets are listed in Table 5. Polarization ratios and OC albedos from as many as five radar experiments per asteroid were averaged to produce these estimates. Note that wherever possible we have used recent literature results to generate updated ellipsoid models (and hence updated $\langle A_{\rm proj}\rangle$ and $\hat{\sigma}_{\rm OC}$) for pre-upgrade experiments, even experiments involving pre-upgrade targets not listed in Table 2. The only noteworthy change in OC albedo is for Kleopatra, for which the pre-upgrade estimate of 0.44 ± 0.15 (Mitchell et al., 1995) has been revised upward to 0.6 ± 0.1.

Updated information on 114 MBA radar experiments carried out between 1980 and March 2003 is included online in Supplementary material, Tables 1, 2, and 3; these are expanded versions of Tables 1, 2, and 4, respectively, describing observations, prior information, and radar properties. All 114 spectra

Table 5
Average radar properties[a]

Target	Class[b]		$\langle\mu_C\rangle$	$\langle\hat{\sigma}_{OC}\rangle$	Note
	Tholen	Bus			
1 Ceres	G	C	0.03 ± 0.03	0.041 ± 0.005	c
2 Pallas	B	B	0.05 ± 0.02	0.075 ± 0.011	c
3 Juno	S	Sk	0.16 ± 0.03	0.14 ± 0.05	
4 Vesta	V	V	0.28 ± 0.05	0.12 ± 0.04	c
5 Astraea	S	S	0.20 ± 0.03	0.20 ± 0.05	c
6 Hebe	S	S	0.00 ± 0.12	0.16 ± 0.05	d
7 Iris	S	S	0.17 ± 0.09	0.13 ± 0.03	e
8 Flora	S	–	0.16 ± 0.05	0.10 ± 0.03	d
9 Metis	S	*T*	0.14 ± 0.04	0.13 ± 0.03	d
12 Victoria	S	L	0.14 ± 0.03	0.22 ± 0.05	c
13 Egeria	G	Ch	0.06 ± 0.05	0.059 ± 0.023	
15 Eunomia	S	S	0.17 ± 0.03	0.085 ± 0.030	
16 Psyche	M	X	0.17 ± 0.05	0.31 ± 0.08	d
18 Melpomene	S	S	0.30 ± 0.08	0.15 ± 0.04	d
19 Fortuna	G	Ch	0.06 ± 0.04	0.074 ± 0.023	d
20 Massalia	S	S	0.28 ± 0.07	0.16 ± 0.06	d
21 Lutetia	M	Xk	0.22 ± 0.07	0.19 ± 0.07	d
22 Kalliope	M	X	0.07 ± 0.10	0.15 ± 0.05	
23 Thalia	S	S	0.19 ± 0.11	0.15 ± 0.06	
25 Phocaea	S	S	0.18 ± 0.03	0.10 ± 0.07	
27 Euterpe	S	S	0.34 ± 0.08	0.10 ± 0.05	c
28 Bellona	S	S	0.32 ± 0.06	0.11 ± 0.04	
31 Euphrosyne	C	Cb	–	<0.058	
33 Polyhymnia	S	Sq	0.07 ± 0.11	0.14 ± 0.07	c
36 Atalante	C	–	0.11 ± 0.03	0.11 ± 0.04	
38 Leda	C	Cgh	0.09 ± 0.08	0.075 ± 0.027	
41 Daphne	C	Ch	0.13 ± 0.08	0.092 ± 0.032	d
46 Hestia	P	Xc	0.09 ± 0.05	0.068 ± 0.015	e
50 Virginia	P	Ch	0.00 ± 0.08	0.085 ± 0.032	
53 Kalypso	PC	–	0.12 ± 0.02	0.20 ± 0.07	
54 Alexandra	C	C	0.08 ± 0.03	0.15 ± 0.05	
60 Echo	S	S	0.17 ± 0.06	0.12 ± 0.04	
66 Maja	C	Ch	0.22 ± 0.12	0.082 ± 0.034	
78 Diana	C	Ch	0.00 ± 0.08	0.13 ± 0.04	c
80 Sappho	S	S	0.25 ± 0.05	0.14 ± 0.05	c
83 Beatrix	M	X	0.23 ± 0.11	0.073 ± 0.026	
84 Klio	G	Ch	0.23 ± 0.06	0.15 ± 0.07	c
85 Io	FC	B	0.00 ± 0.12	0.097 ± 0.037	
88 Thisbe	CF	B	0.00 ± 0.07	0.081 ± 0.028	
97 Klotho	M	–	0.23 ± 0.07	0.21 ± 0.05	d
101 Helena	S	S	0.32 ± 0.09	0.076 ± 0.028	
105 Artemis	C	Ch	0.15 ± 0.04	0.16 ± 0.07	d
109 Felicitas	GC	Ch	0.13 ± 0.03	0.094 ± 0.032	
111 Ate	C	Ch	0.04 ± 0.05	0.16 ± 0.06	
114 Kassandra	T	Xk	0.11 ± 0.06	0.12 ± 0.05	
127 Johanna	CX	Ch	0.18 ± 0.07	0.11 ± 0.05	
128 Nemesis	C	C	0.00 ± 0.07	0.051 ± 0.018	
137 Meliboea	C	–	0.14 ± 0.01	0.21 ± 0.07	
139 Juewa	CP	X	0.10 ± 0.10	0.061 ± 0.025	c
144 Vibilia	C	Ch	0.18 ± 0.10	0.11 ± 0.04	c
145 Adeona	C	Ch	0.03 ± 0.04	0.12 ± 0.04	
182 Elsa	S	S	0.11 ± 0.09	0.13 ± 0.08	
192 Nausikaa	S	Sl	0.19 ± 0.11	0.12 ± 0.03	e
194 Prokne	C	C	0.16 ± 0.04	0.23 ± 0.09	c
198 Ampella	S	S	0.22 ± 0.07	0.26 ± 0.11	
211 Isolda	C	Ch	0.00 ± 0.07	0.15 ± 0.05	
216 Kleopatra	M	Xe	0.00 ± 0.04	0.60 ± 0.15	f
225 Henrietta	F	–	0.26 ± 0.11	0.052 ± 0.021	
230 Athamantis	S	Sl	0.00 ± 0.12	0.22 ± 0.09	c
247 Eukrate	CP	Xc	0.10 ± 0.07	0.039 ± 0.014	
253 Mathilde	C	Cb	0.08 ± 0.02	0.072 ± 0.022	

(*continued in next column*)

Table 5 (*continued*)

Target	Class[b]		$\langle\mu_C\rangle$	$\langle\hat{\sigma}_{OC}\rangle$	Note
	Tholen	Bus			
266 Aline	C	Ch	0.09 ± 0.04	0.21 ± 0.08	
270 Anahita	S	*Sl*	0.26 ± 0.07	0.091 ± 0.039	
288 Glauke	S	S	0.17 ± 0.06	0.17 ± 0.11	g
313 Chaldaea	C	–	0.10 ± 0.03	0.15 ± 0.06	
324 Bamberga	CP	*Cb*	0.11 ± 0.08	0.041 ± 0.019	e
336 Lacadiera	D	Xk	0.16 ± 0.08	0.11 ± 0.04	
354 Eleonora	S	Sl	0.32 ± 0.13	0.15 ± 0.06	
356 Liguria	C	*Ch*	0.12 ± 0.06	0.13 ± 0.05	c
393 Lampetia	C	Xc	0.12 ± 0.02	0.11 ± 0.04	e
405 Thia	C	Ch	0.10 ± 0.03	0.15 ± 0.06	
429 Lotis	C	*Xk*	0.10 ± 0.07	0.066 ± 0.028	
444 Gyptis	C	C	0.09 ± 0.07	0.056 ± 0.026	
488 Kreusa	C	*Ch*	0.14 ± 0.13	0.15 ± 0.06	
505 Cava	FC	–	0.00 ± 0.07	0.066 ± 0.030	
532 Herculina	S	S	0.16 ± 0.11	0.098 ± 0.029	e
554 Peraga	FC	Ch	0.05 ± 0.05	0.20 ± 0.06	e
622 Esther	S	S	0.35 ± 0.09	0.12 ± 0.09	
654 Zelinda	C	Ch	0.13 ± 0.01	0.19 ± 0.05	e
694 Ekard	CP	*Ch*	0.00 ± 0.10	0.095 ± 0.034	d
704 Interamnia	F	B	0.04 ± 0.08	0.059 ± 0.021	
796 Sarita	M	X	–	0.25 ± 0.10	c
914 Palisana	CU	*Ch*	0.44 ± 0.16	0.063 ± 0.025	
1963 Bezovec	C	–	0.06 ± 0.04	0.12 ± 0.07	

[a] Weighted average disk-integrated radar properties from all existing data.

[b] Taxonomic classification on the Tholen system (Tholen, 1989) and the Bus system (Bus and Binzel, 2002a, 2002b) based on visual and infrared data. See footnote a to Table 2 for comments on Tholen classes for 50 Virginia, 53 Kalypso, 83 Beatrix, 127 Johanna, and 253 Mathilde. We follow Rivkin et al. (2000) and Paper I in reassigning 796 Sarita from Tholen class XD to M, based on its visual albedo. Bus classes are listed in italics for eight asteroids that were not classified by Bus and Binzel (2002a, 2002b) but were classified on the Bus system by Lazzaro et al. (2004).

[c] Polarization ratio and OC albedo taken from Paper I.

[d] No new radar data have been obtained for this target, so the polarization ratio is taken from Paper I, but the OC albedo has been updated by using a revised model ellipsoid (not shown) to estimate the mean projected area presented to the radar.

[e] Polarization ratio and OC albedo estimated by combining the radar data and model ellipsoid presented in this paper with the results of earlier radar experiments summarized by Paper I.

[f] Polarization ratio estimated by combining the CW radar data presented in this paper with earlier CW data summarized by Paper I; OC albedo estimated by combining CW-based estimates with delay-Doppler imaging results given by Ostro et al. (2000).

[g] Polarization ratio and OC albedo taken from Ostro et al. (2001).

are displayed online in Supplementary material, Fig. 1, which is an expanded version of Fig. 1.

4. Statistical analyses

4.1. Samples based on Tholen taxonomy

In order to carry out statistical analyses on our 84-asteroid sample, we organize the targets by taxonomic class. The six categories, based on Tholen taxonomy (Tholen, 1989), are C, G (and GC), F (and FC and CF), "PD" (comprising P, D, PC, CP, and CX), S, and M. Four "miscellaneous" targets (2 Pallas [B], 4 Vesta [V], 114 Kassandra [T], and 914 Palisana [CU]) do not fit into any of these categories. Tholen's E, M, and P classes

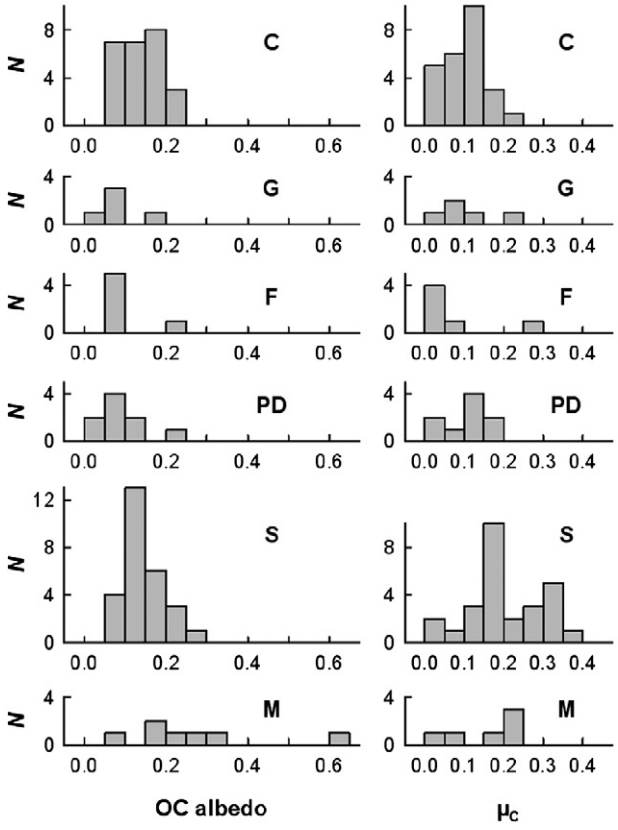

Fig. 3. Histograms of the distributions of the OC albedo $\hat{\sigma}_{OC}$ and polarization ratio μ_C for the C, G, F, PD, S, and M-class samples. Each bin is 0.05 wide and includes the lower but not the upper endpoint.

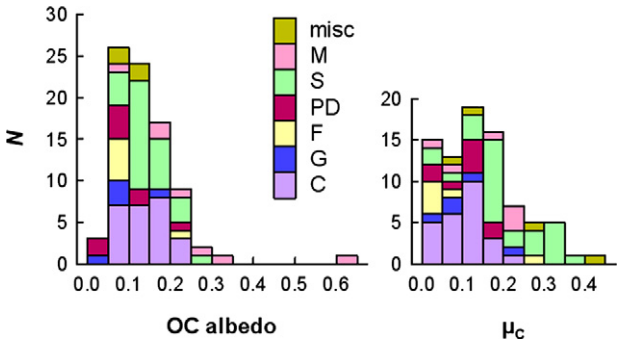

Fig. 4. Histograms of the distributions of the OC albedo $\hat{\sigma}_{OC}$ and polarization ratio μ_C for all MBA radar targets. Each bin is 0.05 wide and includes the lower but not the upper endpoint. Contributions of the various taxonomic classes are indicated.

differ only by visual albedo p_v; if p_v was unknown at the time, Tholen assigned a class of X. For X-class objects that now have visual albedo determinations, we assign them to the appropriate E, M, or P class.

Of our intended survey targets, only one asteroid, 31 Euphrosyne, was not detected. Our upper limit on its OC albedo is only 0.058, so we have chosen to treat this asteroid as a detection at $\hat{\sigma}_{OC} = 0.058$ for statistical purposes, rather than ignoring it altogether or else using involved "survival analysis" techniques (e.g., Magri, 1995) for dealing with limits. Of course we have no idea what Euphrosyne's circular polarization ratio is and hence must omit this target from the sample when considering this parameter.

Fig. 3 shows histograms of the radar albedo and circular polarization ratio distributions for each of our six taxonomic groups, and Fig. 4 shows the distributions for the full sample. Table 6 lists, for each taxonomic category and then for the full sample, the mean μ_C value, the standard deviation, the full range, and the number of targets with measured values, and then the same four quantities for $\hat{\sigma}_{OC}$.

4.2. Linear regressions and principal components analysis

Linear regression analysis can reveal any correlations between μ_C and $\hat{\sigma}_{OC}$, or between either of these two quantities and visual albedo p_v, diameter D, rotation period P, or semimajor axis a. Scatter plots showing the relationships (or lack thereof) between these variables are given in Figs. 5 and 6. Table 7 lists, for each pair of parameters, the probability that the slope of the best-fit line is zero; small numbers imply a high probability of a real trend in the parent population. Probabilities are given for each of the six taxonomic categories separately and then for the full sample. A probability less than 0.05 is often considered to be the threshold at which we can believe a trend; adopting this threshold, it follows that there is one chance in twenty that any given regression will yield a spurious correlation, an apparent trend that in fact results from the luck of the sampling draw rather than from any properties of the parent population. Since our table contains 63 entries we might expect three such spurious correlations.

For the full sample, μ_C is significantly correlated with p_v and is significantly anticorrelated with a; see Fig. 6. This is primarily because the S-class targets in the sample tend to have higher circular polarization ratios, and also tend to have higher visual albedos and smaller semimajor axes, than do the other taxonomic classes. There also is a significant anticorrelation between μ_C and D, but only if the three unusually large targets 1 Ceres, 2 Pallas, and 4 Vesta are excluded from the sample; even then, the trend is not very impressive (Fig. 6). Focusing on individual taxonomic categories, there is a significant anticorrelation between $\hat{\sigma}_{OC}$ and p_v for PD-class objects, and a significant correlation between $\hat{\sigma}_{OC}$ and P for F-class objects; the former trend is messy and the latter trend is entirely due to a single asteroid, 554 Peraga, that has a high OC albedo and a long rotation period. Finally, the correlation between $\hat{\sigma}_{OC}$ and μ_C for G-class targets is significant and strong (Fig. 5); however, we must be careful to remember that there are only five targets here and that we expect a few spurious correlations.

The correlation between polarization ratio and visual albedo for our full sample is the most significant trend in Table 7 in terms of regression probabilities, but in the preceding paragraph we explained it away as a spurious relationship produced by the underlying dependence of both μ_C and p_v on taxonomic class. Could it instead be a real (i.e., causal) physical effect? While we cannot rule this possibility out, we then would expect to see some evidence of this trend within each of our single-class samples, whereas in fact we do not find a significant correlation for any of them.

Table 6
Descriptive statistics

Class	μ_C				$\hat{\sigma}_{OC}$			
	Mean	SD	Range	*N*	Mean	SD	Range	*N*
C	0.098	0.056	0.22	25	0.127	0.050	0.179	26
G	0.102	0.080	0.20	5	0.084	0.042	0.109	5
F	0.058	0.101	0.26	6	0.093	0.055	0.148	6
PD	0.096	0.062	0.18	9	0.090	0.049	0.161	9
S	0.198	0.094	0.35	27	0.140	0.044	0.184	27
M	0.153	0.097	0.23	6	0.255	0.170	0.527	7
misc	0.220	0.176	0.39	4	0.095	0.030	0.057	4
All	0.138	0.098	0.44	82	0.131	0.076	0.561	84

Note. Means, standard deviations, ranges, and sample sizes for polarization ratio and radar albedo, listed as a function of Tholen taxonomic class (Tholen, 1989). Nine asteroids classified as CP, PC, P, and D are grouped here as the "PD" sample. The four miscellaneous objects (2 Pallas, 4 Vesta, 114 Kassandra, and 914 Palisana) are classified as B, V, T, and CU, respectively.

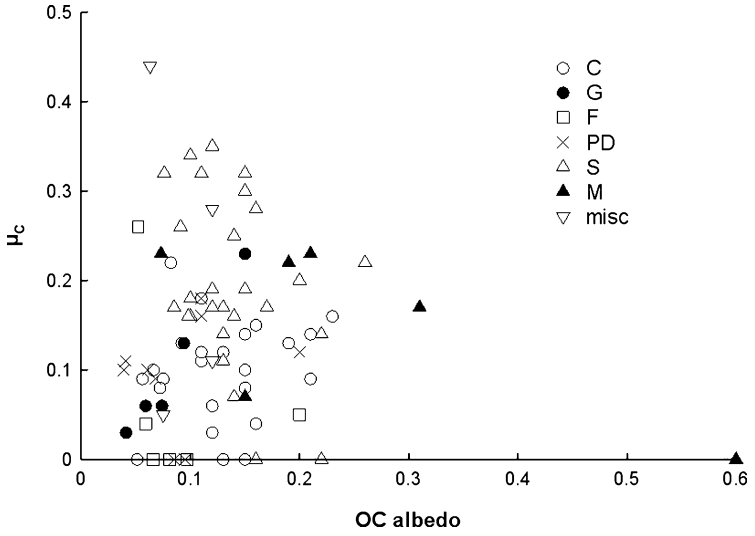

Fig. 5. Polarization ratio μ_C plotted vs OC albedo $\hat{\sigma}_{OC}$ (Table 5). Plotting symbols indicate taxonomic class; see legend. The four miscellaneous objects (2 Pallas, 4 Vesta, 114 Kassandra, and 914 Palisana) are classified as B, V, T, and CU, respectively.

We also dismissed seemingly significant single-class trends simply because we knew in advance that we probably would find some spurious relationships. This, of course, is not a very satisfying approach. For example, we might instead adopt a more stringent probability threshold for individual pairwise regressions such that we would expect less than one spurious trend overall. While we have not formally carried out such a procedure, it is clear from Table 7 that there is only one single-class probability low enough to stand up to such treatment: the correlation between $\hat{\sigma}_{OC}$ and μ_C for G-class targets (see above). So it will be worth testing whether or not this correlation is still significant when we eventually have more than five G-class radar targets.

Paper I noted that, based on five M-class asteroids, there appeared to be an anticorrelation between $\hat{\sigma}_{OC}$ and p_v for that taxon; this trend could have been useful for using visual albedos to identify metallic objects prior to radar detection, since metallic objects have high OC albedo. But Table 7 and Fig. 6 show that the trend is destroyed by the addition of the two new M-class targets 22 Kalliope and 83 Beatrix, both of which have fairly low OC albedo and fairly low visual albedo.

We next attempted principal components analysis on the six variables analyzed above. This method attempts to disentangle the correlations between these variables in order to explain most of the data scatter as variation in a small number of underlying variables, or principal components (e.g., Anderson, 2003). Given the general lack of bivariate correlations discussed above, it is not surprising that principal components analysis was not in fact able to explain most (say, 80%) of the variation in terms of a small number (say, 3) of principal components.

4.3. Multiple comparisons

4.3.1. Overview

In order to determine whether or not the six taxonomic categories have the same average values of $\hat{\sigma}_{OC}$ and μ_C, we carried out Kruskal-Wallis analyses and, when possible, one-way analysis of variance (ANOVA). These two procedures are used to look for differences in the median (Kruskal-Wallis) or mean (ANOVA) for n samples (with $n \geqslant 2$), without the large number of "false positives" (Type I errors) that could arise by naively applying two-sample tests to every one of the $n(n-1)/2$ pairs

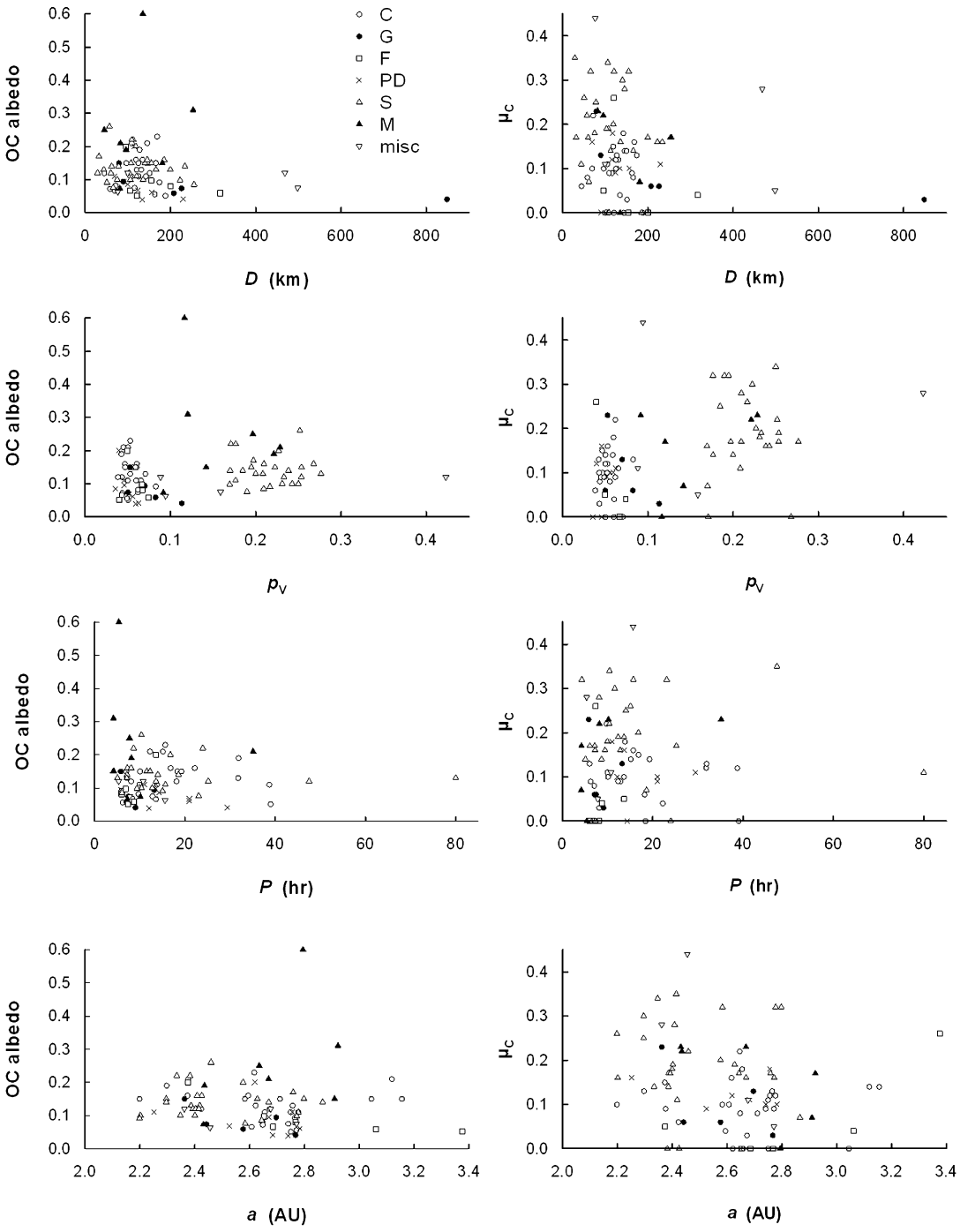

Fig. 6. OC albedo $\hat{\sigma}_{OC}$ and polarization ratio μ_C from Table 5, plotted vs diameter D, visual albedo p_V, rotation period P, and orbital semimajor axis a. Plotting symbols indicate taxonomic class; see legend. The four miscellaneous objects (2 Pallas, 4 Vesta, 114 Kassandra, and 914 Palisana) are classified as B, V, T, and CU, respectively. Error bars have been omitted for clarity; uncertainties on $\hat{\sigma}_{OC}$ and μ_C are listed in Table 5.

of samples. For example, Paper I showed that for $n = 4$, applying six two-sample tests at the usual 5% probability threshold (i.e., treating two means as being equal unless the probability that they are equal is less than 5%) produces an *overall* Type I error rate of 20% rather than 5%: There is a one in five chance that we will find at least one difference between means even if all four parent populations are in fact identical. The Kruskal-Wallis and ANOVA procedures carry out all comparisons simultaneously and yield the probability that *all* medians or means are equal; if this probability is 5%, the probability that at least one median or mean differs from the others is 95%, and the overall Type I error rate is 5%.

The Kruskal-Wallis test (Daniel, 1990, pp. 226–231; Zar, 1996, pp. 197–202) is a rank-based nonparametric procedure for simultaneously comparing the median values of our n categories. For example, if we carry out this test for our six taxonomy-based samples with $\hat{\sigma}_{OC}$ as the variable, and we obtain a low test probability, it follows that at least one of the six

Table 7
Regression probabilities[a]

	Tholen class						
	C	G	F	PD	S	M	*All*
μ_C vs p_v	0.77	0.28	0.094	0.35	0.96	0.41	<0.001[b]
μ_C vs D	0.57	0.24	0.68	0.75	0.32	0.46	0.063[c]
μ_C vs P	0.71[d]	0.79	0.98	0.61	0.76[e]	0.31	0.89[f]
μ_C vs a	0.83	0.29	0.090	0.58	0.94	0.17	0.026[g]
$\hat{\sigma}_{OC}$ vs p_v	0.49	0.17	0.70	0.043[h]	0.94	0.70	0.13
$\hat{\sigma}_{OC}$ vs D	0.90	0.19	0.41	0.18	0.50	0.62	0.11[i]
$\hat{\sigma}_{OC}$ vs P	0.32[j]	0.71	0.039[k]	0.11	0.51[l]	0.66	0.83[m]
$\hat{\sigma}_{OC}$ vs a	0.27	0.19	0.069	0.50	0.93	0.33	0.51
$\hat{\sigma}_{OC}$ vs μ_C	0.44	0.002[n]	0.66	0.62	0.11	0.11	0.72

[a] Probabilities that the null hypothesis of uncorrelated variables is valid. Small values indicate significant correlations between variables.
[b] The μ_C vs p_v trend for all targets has slope 0.52 ± 0.11; the probability is still <0.001 even with the one high-albedo object (4 Vesta) excluded.
[c] The μ_C vs D probability for all targets drops to 0.012, with slope $= (-4.9 \pm 1.9) \times 10^{-3}$ km^{-1}, if the three largest targets (1 Ceres, 2 Pallas, and 4 Vesta) are excluded. The probability remains significant (0.020) if Ceres and the four miscellaneous objects (which include Pallas and Vesta) are excluded.
[d] The μ_C vs P probability for C-class targets stays about the same (0.68) if the long-period target 253 Mathilde is excluded.
[e] The μ_C vs P probability for S-class targets remains high (0.83) even if the long-period target 288 Glauke is excluded.
[f] The μ_C vs P probability for all targets remains high (0.67) even if the long-period targets 253 Mathilde and 288 Glauke are excluded.
[g] The μ_C vs a trend for all targets has slope $= -0.105 \pm 0.046$ AU^{-1}. The trend is no longer significant (probability = 0.062) if the four miscellaneous objects are excluded.
[h] The $\hat{\sigma}_{OC}$ vs p_v trend for PD-class targets has slope $= -3.9 \pm 1.5$.
[i] The $\hat{\sigma}_{OC}$ vs D probability for all targets is high (0.43) even if the three largest targets (1 Ceres, 2 Pallas, and 4 Vesta) are excluded.
[j] The $\hat{\sigma}_{OC}$ vs P probability for C-class targets is high (0.68) even if the long-period target 253 Mathilde is excluded.
[k] The $\hat{\sigma}_{OC}$ vs P trend for F-class targets has slope $= 0.017 \pm 0.006$ h^{-1}; the trend is due mostly to one target, 554 Peraga.
[l] The $\hat{\sigma}_{OC}$ vs P probability for S-class targets remains high (0.60) even if the long-period target 288 Glauke is excluded.
[m] The $\hat{\sigma}_{OC}$ vs P probability for all targets remains high (0.62) even if the long-period targets 253 Mathilde and 288 Glauke are excluded.
[n] The $\hat{\sigma}_{OC}$ vs μ_C trend for G-class targets has slope $= 0.51 \pm 0.05$.

parent populations probably has a different median OC albedo than the others. The Kruskal-Wallis test, however, does not identify which medians are different from which other medians; to learn about this we then use the Dunn post hoc test (Zar, 1996, p. 227).

Since ANOVA has somewhat higher power than does the Kruskal-Wallis test—that is, better ability to identify differences if differences actually exist between the n parent populations—it also would be helpful to carry out this procedure if possible. It gives us the probability that all n population means for the variable under consideration are equal, under the assumption that this variable is normally distributed for each population and that all n populations have the same variance. (Strictly speaking, the Kruskal-Wallis test also assumes equal variances, but it is often considered to be insensitive to violations of this assumption; see, however, Zimmerman, 2000.) We use the Shapiro–Wilk test (Conover, 1980, pp. 363–366) to check whether or not the distributions are normal, and Levene's test (Snedecor and Cochran, 1980, pp. 253–254) to check for equal variances. If either test indicates a low probability that the corresponding assumption is valid, the only way to perform ANOVA is to find a data transformation that corrects the problem.

When a statistical test on some variable relies on an assumption about how that variable is distributed for the parent populations—say, that it is a normal distribution, or that the distributions have equal variance—and this assumption is violated, it is standard practice to seek a data transformation such that the transformed variable obeys the assumption (e.g., Zar, 1996, pp. 273–281; Snedecor and Cochran, 1980, pp. 282–297). We might take the square root of all data values, or the inverse sine, or the logarithm. (Astronomers implicitly use a logarithmic transformation whenever they analyze magnitude data.) If, for example, Levene's test shows that our six Tholen-based populations have different variances in $\hat{\sigma}_{OC}$, we must seek a transformation that brings the six variances closer together *without* skewing the six distributions to the point where some of them are no longer approximately normal.

If the two assumptions of normality and equal variances can be met then we can run ANOVA. A low test probability implies that at least one of the n population means is probably different than the others; but just as with the Kruskal-Wallis test, we need a post hoc test to tell us which means differ from which other means. A number of such post hoc tests are available, but here we will just use one, the Tukey "honestly significant difference" test (Zar, 1996, pp. 212–218); this test is moderately conservative, meaning (hopefully) that we will not identify differences that are not real (too liberal) but will not ignore differences that actually exist in the parent populations (too conservative).

4.3.2. Results

The result of running a Kruskal-Wallis test for the $\hat{\sigma}_{OC}$ variable is a tiny probability, less than 0.001, that the six median OC albedos for our six Tholen-based populations are equal. The Dunn post hoc test (Zar, 1996, p. 227) then shows (Table 8) that, as we expected, there is a high probability that M-class targets have different (higher) median OC albedos than do G-, F-, and PD-class targets. No other differences are significant at the 95% confidence level.

Table 8
Multiple comparisons

Variable	Shapiro–Wilk		Levene	K-W	Dunn					ANOVA	Tukey HSD				
	C G F	PD S M			C–G C–F C–PD	C–S C–M G–F	G–PD G–S G–M	F–PD F–S F–M	PD–S PD–M S–M		C–G C–F C–PD	C–S C–M G–F	G–PD G–S G–M	F–PD F–S F–M	PD–S PD–M S–M
$\hat{\sigma}_{OC}$	0.32	0.12	0.021	0.001	1	1	1	1	0.13	–	–	–	–	–	–
	0.60	0.039			1	0.34	0.36	0.36	0.009		–	–	–	–	–
	0.023	0.15			0.78	1	0.030	0.028	1		–	–	–	–	–
$\ln \hat{\sigma}_{OC}$	0.21	0.77	0.40	0.001	1	1	1	1	0.13	<0.001	0.40	0.67	1	1	0.029
	1	0.80			1	0.34	0.36	0.36	0.009		0.59	0.008	0.085	0.14	<0.001
	0.29	0.95			0.78	1	0.030	0.028	1		0.28	1	0.001	0.002	0.11
$\hat{\sigma}_{OC} - \hat{\sigma}_{SC}$	0.33	0.097	0.026	0.012	0.67	1	1	1	0.63	–	–	–	–	–	–
	0.89	0.030			1	1	0.86	1	0.060		–	–	–	–	–
	0.13	0.044			0.46	1	0.092	0.23	1		–	–	–	–	–
$\ln(\hat{\sigma}_{OC} - \hat{\sigma}_{SC})$	0.11	0.53	0.56	0.012	0.67	1	1	1	0.63	0.003	0.47	1	1	1	0.24
	1	0.86			1	1	0.86	1	0.060		0.77	0.096	0.35	0.64	0.005
	0.91	0.76			0.46	1	0.092	0.23	1		0.37	1	0.013	0.032	0.16
$\hat{\sigma}_{OC} - 2\hat{\sigma}_{SC}$	0.21	0.28	0.033	0.061	–	–	–	–	–	–	–	–	–	–	–
	0.93	0.031			–	–	–	–	–		–	–	–	–	–
	0.41	0.013			–	–	–	–	–		–	–	–	–	–
$\ln(\hat{\sigma}_{OC} - 2\hat{\sigma}_{SC})$	0.056	0.81	0.51	0.061	–	–	–	–	–	0.13	–	–	–	–	–
	0.74	0.98			–	–	–	–	–		–	–	–	–	–
	0.95	0.72			–	–	–	–	–		–	–	–	–	–
$\hat{\sigma}_{OC} - 3\hat{\sigma}_{SC}$	0.39	0.26	0.018	0.042	0.58	0.10	1	1	1	–	–	–	–	–	–
	0.79	0.012			1	1	1	1	1		–	–	–	–	–
	0.78	0.005			1	1	1	1	0.95		–	–	–	–	–
$\ln(\hat{\sigma}_{OC} - 3\hat{\sigma}_{SC} + 0.05)$	0.30	0.54	0.032	0.042	0.58	0.10	1	1	1	–	–	–	–	–	–
	0.77	0.49			1	1	1	1	1		–	–	–	–	–
	0.94	0.36			1	1	1	1	0.95		–	–	–	–	–
μ_C	0.51	0.21	0.47	<0.001	1	0.002	1	1	0.077	–	–	–	–	–	–
	0.26	0.14			1	1	0.45	0.009	1		–	–	–	–	–
	0.003	0.11			1	1	1	0.63	1		–	–	–	–	–
$\sqrt{\mu_C}$	0.001	0.006	0.79	<0.001	1	0.002	1	1	0.077	–	–	–	–	–	–
	0.55	<0.001			1	1	0.45	0.009	1		–	–	–	–	–
	0.078	0.031			1	1	1	0.63	1		–	–	–	–	–

Note. The six samples analyzed here are described in Table 6. For each variable, probabilities derived from various statistical tests are listed: the Shapiro–Wilk normality test (for each of our six samples), Levene's test for equal variances, the Kruskal-Wallis (K-W) rank-order multiple-sample test, Dunn's post hoc test (performed after the Kruskal-Wallis test for each pair of samples), the one-way unblocked analysis of variance (ANOVA) multiple-sample test, and Tukey's "honestly significant difference" (HSD) post hoc test (performed after ANOVA for each pair of samples). See text for a description of each test. Low probabilities (conventionally taken to mean less than 0.05) imply that the parent populations in question probably differ from each other or (for the Shapiro–Wilk test) from the normal distribution. The power of the $\ln(\hat{\sigma}_{OC} - 2\hat{\sigma}_{SC})$ ANOVA test is only 0.25: There is only a 0.25 probability of detecting a real difference in means at the 95% confidence level. That is, the test is very insensitive. The conventional minimum acceptable power is 0.80, so the negative test result (probability >0.05) obtained here could be incorrect.

Before carrying out ANOVA for $\hat{\sigma}_{OC}$ we ran Levene's test to check for equal population variances. At the top of Table 8 we see that this test yields a 0.021 probability that the six variances are equal, which is well below our 0.05 threshold. This is not surprising, given that the M-class standard deviation is about three times larger than those for the G, F, and PD categories (Table 6). A logarithmic transformation turns out to remedy this problem: We see in the second row of Table 8 that there is a 0.40 probability that all six variances in $\ln \hat{\sigma}_{OC}$ are equal.

We also ran the Shapiro–Wilk test to check whether or not the assumption of normal distributions is valid. We see in Table 8 that F- and S-class distributions in $\hat{\sigma}_{OC}$ are unlikely to be normal, but that the same logarithmic transformation that made the variances similar to each other also raised all six Shapiro–Wilk probabilities above the 0.05 threshold.

Hence we can perform ANOVA on the $\ln \hat{\sigma}_{OC}$ variable, with the result that there is only a 0.001 probability that the six population means are equal to each other. The Tukey "honestly significant different" post hoc test then finds the same differences that the Dunn post hoc test did—M-class albedos higher than those from the G, F, and PD categories—plus it finds that M-class albedos are higher than C-class albedos and that S-class albedos are higher than PD-class albedos. Neither test finds (at the 95% confidence level) a difference between M-class and S-class albedos.

We can perform the same analyses on the logarithm of the variable $\hat{\sigma}_{OC} - \hat{\sigma}_{SC}$ $(= \hat{\sigma}_{OC}[1 - \mu_C])$, which represents an attempt to remove the effects of diffuse radar scattering on the assumption that such scattering produces a randomly polarized echo. That is, it is an attempt to obtain the radar albedo due solely to quasispecular scattering. Again we find that a logarithmic transformation is needed before we can perform ANOVA, and again we find that at the 95% confidence level the six medians (Kruskal-Wallis) or means (ANOVA) are not all equal. Yet although the Kruskal-Wallis test shows that at least one median differs from the others, the Dunn post hoc test is unable to identify any such median at 95% confidence, although it comes close when comparing the M class to the PD category (Table 8). The Tukey post hoc test is able to show that these two means differ with high confidence, and also that the M class differs from the G and F classes.

Another way to obtain the quasispecular albedo would be to compute $\hat{\sigma}_{OC} - 2\hat{\sigma}_{SC}$, on the assumption, based on studies of the Moon and inner planets, that diffusely scattered radiation has a circular polarization ratio of 0.5 rather than 1.0 (see Paper I and references therein). However, we find that the tests performed on our sample for the logarithm of this variable have low statistical power—that is, these tests are insensitive to actual differences between the parent populations—so the tabulated results must be treated with caution.

Having dealt with radar albedo, we now consider circular polarization ratio. Kruskal-Wallis indicates that S-class asteroids have higher average μ_C than do C- or F-class asteroids. We cannot perform ANOVA for this variable because the F-class distribution is not normal; as shown in the last line of Table 8, a square-root transformation improves this situation but only at the expense of skewing four of the other five distributions.

One might suppose that the high S-class polarization ratios would mean that S-class radar albedos, after correction for diffuse scattering $(\hat{\sigma}_{OC} - \hat{\sigma}_{SC})$, would be lower than corrected C-class albedos, contrary to the results discussed earlier. But since this correction is a first-order effect, and since the uncorrected S-class OC albedos are slightly higher than for the C class (see Table 6), the mean values of $\hat{\sigma}_{OC} - \hat{\sigma}_{SC}$ for the two samples are almost identical (0.116 for C vs 0.113 for S).

4.4. Samples with the BFGPTD classes combined

In order to make a more direct comparison with the results of Paper I we also carried out Kruskal-Wallis and ANOVA with all dark asteroids outside the C taxon—B-, F-, G-, P-, T-, and D-class targets—combined into a "BFGPTD" class. (Paper I used a "BFGP" class, since their 37 radar-detected targets did not include any T- or D-class objects.) Our results can be viewed in Tables 9 and 10. Average S-class polarization ratios are higher than those for C and BFGPTD, consistent with the discussion above; Paper I did not find this trend to be statistically significant, despite the fact that it was suggested by visual inspection of histograms. Kruskal-Wallis analysis of $\ln \hat{\sigma}_{OC}$ indicates that BFGPTD asteroids are darker than S- and M-class asteroids; ANOVA confirms this and further implies that BFGPTD objects are darker than C-class objects and that both C- and S-class targets are darker than M-class objects. This again broadly agrees with the results of Paper I, which found that M-class asteroids are more radar bright than others, that C- and S-class objects have similar radar albedo distributions, and (tentatively) that BFGP objects are less radar bright than other asteroids.

Interestingly, when we attempt to remove diffuse scattering by analyzing $\ln(\hat{\sigma}_{OC} - \hat{\sigma}_{SC})$ rather than $\ln \hat{\sigma}_{OC}$, the major change is that we no longer can state that M-class objects are brighter than C- and S-class targets. The two newly detected M-class targets, 22 Kalliope and (especially) 83 Beatrix, are

Table 9
Descriptive statistics with BFGPTD class

Class	μ_C				$\hat{\sigma}_{OC}$			
	Mean	SD	Range	*N*	Mean	SD	Range	*N*
C	0.098	0.056	0.22	25	0.127	0.050	0.179	26
BFGPTD	0.086	0.074	0.26	22	0.090	0.045	0.161	22
S	0.198	0.094	0.35	27	0.140	0.044	0.184	27
M	0.153	0.097	0.23	6	0.255	0.170	0.527	7

Note. Means, standard deviations, ranges, and sample sizes for polarization ratio and radar albedo, listed as a function of Tholen taxonomic class (Tholen, 1989). Twenty-two asteroids classified as B, F, FC, CF, G, GC, P, CP, PC, T, and D are grouped here as the "BFGPTD" sample.

Table 10
Multiple comparisons with BFGPTD class

Variable	Shapiro–Wilk		Levene	K-W	Dunn			ANOVA	Tukey HSD		
	C BFGPTD	S M			C–B C–S	C–M B–S	B–M S–M		C–B C–S	C–M B–S	B–M S–M
$\hat{\sigma}_{OC}$	0.32 0.005	0.039 0.15	0.003	<0.001	0.051 1	0.14 0.002	<0.001 0.60	–	– –	– –	– –
$\ln \hat{\sigma}_{OC}$	0.21 0.56	0.80 0.95	0.16	<0.001	0.051 1	0.14 0.003	<0.001 0.60	<0.001	0.019 0.65	0.006 <0.001	<0.001 0.050
$\hat{\sigma}_{OC} - \hat{\sigma}_{SC}$	0.33 0.006	0.030 0.044	0.004	0.002	0.030 1	0.83 0.046	0.007 0.64	–	– –	– –	– –
$\ln(\hat{\sigma}_{OC} - \hat{\sigma}_{SC})$	0.11 0.51	0.86 0.76	0.29	0.002	0.030 1	0.83 0.046	0.007 0.64	<0.001	0.021 1	0.081 0.025	<0.001 0.066
$\hat{\sigma}_{OC} - 2\hat{\sigma}_{SC}$	0.21 0.009	0.031 0.013	0.007	0.019	0.068 0.70	1 1	0.078 0.38	–	– –	– –	– –
$\ln(\hat{\sigma}_{OC} - 2\hat{\sigma}_{SC})$	0.056 0.72	0.98 0.72	0.41	0.019	0.068 0.70	1 1	0.078 0.38	0.006	0.071 0.42	0.36 0.73	0.011 0.053
$\hat{\sigma}_{OC} - 3\hat{\sigma}_{SC}$	0.39 0.031	0.012 0.005	0.004	0.019	0.20 0.038	1 1	0.73 0.37	–	– –	– –	– –
$\ln(\hat{\sigma}_{OC} - 3\hat{\sigma}_{SC} + 0.05)$	0.30 0.85	0.49 0.36	0.016	0.019	0.20 0.038	1 1	0.73 0.37	–	– –	– –	– –
μ_C	0.51 0.067	0.14 0.11	0.19	<0.001	1 0.001	0.77 <0.001	0.40 1	<0.001	0.94 <0.001	0.42 <0.001	0.25 0.59
$\sqrt{\mu_C}$	0.001 0.046	<0.001 0.031	0.50	<0.001	1 0.001	0.77 <0.001	0.40 1	–	– –	– –	– –

Note. The four samples analyzed here are described in Table 9. For each variable, probabilities derived from various statistical tests are listed: see footnote to Table 8 for descriptions of column entries. For the Dunn and Tukey "honestly significant difference" (HSD) post hoc tests, column label "B" stands for the "BFGPTD" sample (see text). The power of the $\ln(\hat{\sigma}_{OC} - 2\hat{\sigma}_{SC})$ ANOVA test is only 0.75: There is only a 0.75 probability of detecting a real difference in means at the 95% confidence level. That is, the test is somewhat insensitive—the conventional minimum acceptable power is 0.80—although it indicates a significant difference (probability <0.05) anyway.

Table 11
Descriptive statistics for Bus taxonomy

Class	μ_C				$\hat{\sigma}_{OC}$			
	Mean	SD	Range	*N*	Mean	SD	Range	*N*
C	0.072	0.061	0.16	5	0.106	0.082	0.189	5
Ch	0.099	0.074	0.23	18	0.129	0.045	0.151	18
B–Cb	0.034	0.034	0.08	5	0.074	0.015	0.039	6
Dark X	0.113	0.025	0.07	6	0.085	0.033	0.081	6
S	0.217	0.090	0.35	18	0.137	0.045	0.184	18
Medium X	0.138	0.100	0.23	5	0.262	0.184	0.527	6

Note. Means, standard deviations, ranges, and sample sizes for polarization ratio and radar albedo, listed as a function of Bus taxonomic class (Bus and Binzel, 2002b). Six asteroids that have low visual albedo and are classified as X, Xc, and Xk are grouped here as the "dark X" sample. Six asteroids that have moderate visual albedo and are classified as X, Xe, and Xk are grouped here as the "medium X" sample.

not particularly radar bright, thus lowering the mean for this taxon and bringing it closer to the means for the C and S taxa. On the other hand, the large *standard deviation* of the M-class albedo distribution—triple that of any other albedo distribution—clearly sets this taxon apart from all others, just as Paper I found for their smaller sample.

4.5. Samples based on Bus taxonomy

Finally we attempted similar analyses using the Bus taxonomy (Bus and Binzel, 2002a, 2002b) rather than the Tholen taxonomy. Bus taxonomic types for 67 of our targets were obtained from the NASA Planetary Data System Small Bodies Node (http://www.psi.edu/pds/archive/tax.html); adding eight more classifications from the S^3OS^2 survey (Lazzaro et al., 2004) did not significantly change our results. We created six taxonomic groups in order to have reasonable numbers of objects in each group: C, Ch, combined B and Cb, "dark X" (X, Xk, and Xc with low visual albedo), S, and "medium X" (X, Xk, and Xe with moderate visual albedo). Eight miscellaneous objects with types Cgh, L, Sk, Sl, Sq, and V were omitted from the analysis.

Our results are listed in Tables 11 and 12. In accord with what has already been discussed above, S-class polarization ratios are higher on average than those of the C, Ch, and B/Cb classes. In analyzing OC albedos we must again use a logarithmic transformation to deal with the particularly small variance in the B/Cb class. Having done this, we find via the Kruskal-Wallis test that the "medium X" class has higher mean OC albedo than does B/Cb, while ANOVA also reveals a distinction between "medium X" and both C and "dark X." These results also are in general accord with our findings based on Tholen taxonomy.

We suspect that a larger sample would yield more interesting results based on Bus taxonomy. Just as we have not demonstrated statistically significant differences between, say, the F and G Tholen classes, we have not been able to distinguish between the C and Ch Bus classes; just as we were forced in Paper I to combine several Tholen classes into a combined "BFGP" class, we were forced in the present study to combine several Bus classes at a time for statistical purposes. Fine distinctions between the various Bus taxa probably will not be revealed until we can compare, say, eight C objects with six Ch objects with seven Xc objects, etc.

5. Discussion

Analysis of our sample of 84 radar-observed asteroids has confirmed two of the main conclusions that Paper I reached using a 37-target sample: C- and S-class asteroids have indistinguishable radar albedo distributions; and M-class asteroids have a particularly wide albedo distribution with a somewhat high mean albedo. Since C-class asteroids are presumably the parent bodies of carbonaceous chondrites, the similarity of C- and S-class radar albedos is in accord with S-class NEA 433 Eros being made of ordinary chondritic material (e.g., Cheng, 2002) rather than denser stony-iron material. We can understand our M-class result by noting that while some of these objects are metal-rich—for example, 216 Kleopatra (Ostro et al., 2000)—others probably are not. Five of our seven M-class targets have been observed spectroscopically at 3 μm (Rivkin et al., 2000); of these five, the two with moderate OC albedo (21 Lutetia and 22 Kalliope) are hydrated and hence not metal-rich, while the three with high or moderately high OC albedo (16 Psyche, 216 Kleopatra, and 796 Sarita) show no sign of hydration. Additional evidence that not all M-class objects are metallic comes from observations of the Kalliope binary system (Margot and Brown, 2003), which indicate a volume-averaged bulk density of only $2.4 \pm 0.4\ \mathrm{g\,cm^{-3}}$, much too low to be easily reconciled with an iron/nickel composition.

Paper I also made the tentative suggestion that dark asteroids outside the C taxon—that is, those in the B, F, G, and P classes—may have lower radar albedos than C-class (and S-class) objects. In the present work we first considered the F, G, and PD classes taken separately, and none of our tests show a distinction between these and C-class objects. (Our ANOVA analysis did turn up a distinction between S and PD albedos.) This implies that the alleged distinction is on shaky ground. However, when we then combined the F, G, and PD classes (plus one object each in the B and T classes) for statistical purposes, much as Paper I did, we found that the resulting BFGPTD class does indeed have lower mean radar albedo than C- and S-class objects. It may simply be the case that more radar-detected objects in each individual taxon are needed before we can see this effect when considering these taxa separately; for example, a followup radar survey of dark MBAs, carried out by the present authors and E. Howell, should improve the situation for these classes.

Table 12
Results of multiple comparisons for Bus taxonomy

Variable	Shapiro–Wilk		Levene	K-W	Dunn					ANOVA	Tukey HSD				
	C	dX			C–Ch	C–S	Ch–dX	B–dX	dX–S		C–Ch	C–S	Ch–dX	B–dX	dX–S
	Ch	S			C–B	C–mX	Ch–S	B–S	dX–mX		C–B	C–mX	Ch–S	B–S	dX–mX
	B–Cb	mX			C–dX	Ch–B	Ch–mX	B–mX	S–mX		C–dX	Ch–B	Ch–mX	B–mX	S–mX
$\hat{\sigma}_{OC}$	0.13	0.30	0.004	0.002	1	1	0.90	1	0.42	–	–	–	–	–	–
	0.55	0.11			1	0.25	1	0.060	0.058		–	–	–	–	–
	0.61	0.32			1	0.16	1	0.009	1		–	–	–	–	–
$\ln\hat{\sigma}_{OC}$	0.26	0.28	0.058	0.002	1	1	0.90	1	0.42	<0.001	0.52	0.33	0.28	1	0.14
	0.68	0.98			1	0.25	1	0.060	0.058		0.99	0.008	1	0.58	0.002
	0.66	1			1	0.16	1	0.009	1		1	0.13	0.075	<0.001	0.16
$\hat{\sigma}_{OC} - \hat{\sigma}_{SC}$	0.12	0.56	0.018	0.055	–	–	–	–	–	–	–	–	–	–	–
	0.34	0.26			–	–	–	–	–		–	–	–	–	–
	0.91	0.15			–	–	–	–	–		–	–	–	–	–
$\ln(\hat{\sigma}_{OC} - \hat{\sigma}_{SC})$	0.19	0.43	0.16	0.055	–	–	–	–	–	0.012	0.66	0.84	0.30	1	0.50
	0.53	0.98			–	–	–	–	–		1	0.058	1	0.71	0.016
	0.99	0.92			–	–	–	–	–		1	0.51	0.29	0.036	0.16
$\hat{\sigma}_{OC} - 2\hat{\sigma}_{SC}$	0.12	0.87	0.021	0.13	–	–	–	–	–	–	–	–	–	–	–
	0.18	0.39			–	–	–	–	–		–	–	–	–	–
	0.72	0.069			–	–	–	–	–		–	–	–	–	–
$\ln(\hat{\sigma}_{OC} - 2\hat{\sigma}_{SC})$	0.19	0.65	0.24	0.13	–	–	–	–	–	0.049	0.86	1	0.44	1	0.99
	0.32	0.78			–	–	–	–	–		1	0.26	0.49	1	0.078
	0.87	0.95			–	–	–	–	–		1	0.85	0.61	0.26	0.080
$\hat{\sigma}_{OC} - 3\hat{\sigma}_{SC}$	0.64	0.99	0.021	0.080	–	–	–	–	–	–	–	–	–	–	–
	0.14	0.12			–	–	–	–	–		–	–	–	–	–
	0.47	0.030			–	–	–	–	–		–	–	–	–	–
$\ln(\hat{\sigma}_{OC} - 3\hat{\sigma}_{SC} + 0.05)$	0.090	0.96	0.053	0.080	–	–	–	–	–	0.019	0.98	0.85	0.70	0.99	0.99
	0.23	0.34			–	–	–	–	–		1	0.55	0.067	0.82	0.21
	0.53	0.68			–	–	–	–	–		0.99	0.99	0.72	0.57	0.021
μ_C	0.86	0.15	0.10	<0.001	1	0.036	1	1	0.49	<0.001	0.98	0.006	1	0.52	0.061
	0.31	0.20			1	1	0.008	0.002	1		0.97	0.74	<0.001	<0.001	0.99
	0.42	0.39			1	1	1	0.73	1		0.95	0.55	0.91	0.27	0.33
$\sqrt{\mu_C}$	0.72	0.24	0.41	<0.001	1	0.036	1	1	0.49	–	–	–	–	–	–
	0.070	0.001			1	1	0.008	0.002	1		–	–	–	–	–
	0.15	0.16			1	1	1	0.73	1		–	–	–	–	–

Note. The six samples analyzed here are described in Table 11. For each variable, probabilities derived from various statistical tests are listed: see footnote to Table 8 for descriptions of column entries. Column labels "dX" and "mX" stand for the "dark X" and "medium X" samples, respectively (see text). For the Dunn and Tukey "honestly significant difference" (HSD) post hoc tests, column label "B" stands for the "combined B and Cb" sample. The power of the $\ln(\hat{\sigma}_{OC} - 2\hat{\sigma}_{SC})$ ANOVA test is only 0.45: There is only a 0.45 probability of detecting a real difference in means at the 95% confidence level. That is, the test is very insensitive—the conventional minimum acceptable power is 0.80—so the borderline test result (probability ∼0.05) obtained here may overestimate the probability that all six population means are identical. The power of the $\ln(\hat{\sigma}_{OC} - \hat{\sigma}_{SC})$ and $\ln(\hat{\sigma}_{OC} - 3\hat{\sigma}_{SC})$ ANOVA tests is only 0.69 and 0.62, respectively: These tests are somewhat insensitive, although they indicate significant differences (probability <0.05) anyway.

We also find that a second tentative suggestion made in Paper I is probably incorrect: The radar albedos and visual albedos of M-class asteroids are *not* significantly anticorrelated. It is not terribly surprising that this result has changed, given that the number of M-class radar albedos available as of 1999 was only 5. The number analyzed here is still only 7, but an ongoing radar survey of M-class targets (M. Shepard, personal communication) is in the process of further increasing this figure. For the time being it seems safe to say, as discussed above, that M-class targets have a wide range of radar albedos, including some particularly high albedos, and that this results from the fact that some of these asteroids are metal-rich while others are not.

Our final comparison with Paper I involves circular polarization ratios. The earlier study noted that the μ_C distributions for the various taxa were statistically indistinguishable, even though visual inspection of histograms seemed to imply a particularly high mean polarization ratio for S-class asteroids. In the present study, our larger sample has enabled us to confirm that the mean S-class ratio is higher than those for the C and F classes. In other words, the near-surface region of S-class MBAs—the region within a meter or so of the surface—tends to be particularly rough (structurally complex) at decimeter scales, due to surface rocks, buried rocks, subsurface voids, etc. This difference might be due to differences in material strength, since the carbon-rich material of which C-class objects are composed might more easily be comminuted to a fine regolith that produces low-μ_C radar echoes. It would be difficult to explain low M-class ratios that way, but so far we find no direct statistical evidence for a distinction between S and M in this regard. Alternatively, one could invoke a different impactor population in the inner main belt (where S-class objects tend to be located) vs the middle and outer belt. A third possibility is that S-class material has a particularly high (or low) loss tangent and hence a particularly low (or high) radar penetration depth; in this scenario, the mean polarization ratios are different because the degree of decimeter-scale structure varies with depth and the radar probes to different depths for different taxa.

The large sample analyzed here has enabled us to consider the F, G, and PD classes separately, rather than using a coarser "BFGP" class as did Paper I. However, this approach has for the most part failed to reveal important differences between the radar properties of these dark asteroid classes. As mentioned earlier, this may change when we have more than a handful of radar-detected objects in each of these classes. For example, it is intriguing that the F-class OC albedo distribution (see Fig. 3) has just one object, 554 Peraga, whose albedo is not extremely low; as more F-class radar detections are obtained, it will be interesting to see whether Peraga is truly an unusual object in this respect.

It can be seen that our overall conclusions are not so very different from those of Paper I, and since there are now a reasonable number of radar-detected C- and S-class MBAs, it is likely that future modifications will only occur as we build up detections of targets in the M-class, F-class, etc.—a slow process, given that these are rarer asteroids, and given that the inverse fourth power dependence of echo strength on distance means that we can only profitably observe reasonably large MBAs that happen to reach opposition reasonably close to Earth while located within the Arecibo declination window. Hence statistical conclusions based on CW radar data are not likely to change much in the near future.

Acknowledgments

We thank the Arecibo technical staff for its help with the observations, Ellen Howell for helpful discussions, and the two anonymous reviewers for their comments. C. Magri was partially supported by NSF Grant AST-0205975. The Arecibo Observatory is part of the National Astronomy and Ionosphere Center, which is operated by Cornell University under a cooperative agreement with the National Science Foundation. Part of this research was conducted at the Jet Propulsion Laboratory, California Institute of Technology, under contract with the National Aeronautics and Space Administration (NASA). This material is based in part upon work supported by NASA under the Science Mission Directorate Research and Analysis Programs.

Supplementary material

The online version of this article contains additional supplementary material.

Please visit DOI: 10.1016/j.icarus.2006.08.018.

References

Anderson, T.W., 2003. An Introduction to Multivariate Statistical Analysis, third ed. Wiley, New York, pp. 459–486.

Binzel, R.P., Burbine, T.H., Bus, S.J., 1996. Groundbased reconnaissance of Asteroid 253 Mathilde: Visible wavelength spectrum and meteorite comparison. Icarus 119, 447–449.

Blanco, C., Riccioli, D., 1998. Pole coordinates and shape of 30 asteroids. Astron. Astrophys. Suppl. Ser. 131, 385–394.

Blanco, C., Cigna, M., Riccioli, D., 2000. Pole and shape determination of asteroids. II. Planet. Space Sci. 48, 973–982.

Bowell, E., Gehrels, T., Zellner, B., 1979. Magnitudes, colors, types and adopted diameters of the asteroids. In: Gehrels, T. (Ed.), Asteroids. Univ. of Arizona Press, Tucson, pp. 1108–1129.

Brown, R.H., Morrison, D., 1984. Diameters and albedos of thirty-six asteroids. Icarus 59, 20–24.

Bus, S.J., Binzel, R.P., 2002a. Phase II of the Small Main-Belt Asteroid Spectroscopic Survey: The observations. Icarus 158, 106–145.

Bus, S.J., Binzel, R.P., 2002b. Phase II of the Small Main-Belt Asteroid Spectroscopic Survey: A feature-based taxonomy. Icarus 158, 146–177.

Cellino, A., Diolaiti, E., Ragazzoni, R., Hestroffer, D., Tanga, P., Ghedina, A., 2003. Speckle interferometry observations of asteroids at TNG. Icarus 162, 278–284.

Cheng, A.F., 2002. Near Earth Asteroid Rendezvous: Mission summary. In: Bottke, W.F., Cellino, A., Paolicchi, P., Binzel, R.P. (Eds.), Asteroids III. Univ. of Arizona Press, Tucson, pp. 351–366.

Conover, W.J., 1980. Practical Nonparametric Statistics, second ed. Wiley, New York.

Daniel, W.W., 1990. Applied Nonparametric Statistics, second ed. PWS–Kent, Boston.

Dotto, E., Barucci, M.A., Müller, T.G., Brucato, J.R., Fulchignoni, M., Mennella, V., Colangeli, L., 2002. ISO observations of low and moderate albedo asteroids: PHT-P and PHT-S results. Astron. Astrophys. 393, 1065–1072.

Dunham, D.W., 2003. Observed minor planet occultation events. Online at http://mpocc.astro.cz/world/mpocc1.txt, accessed 2003 November 16.

Dunham, D.W., Goffin, E., Manek, J., Federspiel, M., Stone, R., Owen, W., 2002. Asteroidal occultation results multiply helped by HIPPARCOS. Mem. Soc. Astron. Ital. 73, 662–665.

Erikson, A., Berthier, J., Denchev, P.V., Harris, A.W., Ioannou, Z., Kryszczynska, A., Lagerkvist, C.-I., Magnusson, P., Michalowski, T., Nathues, A., Piironen, J., Pravec, P., Šarounová, L., Velichko, F., 1999. Photometric observations and modeling of the Asteroid 85 Io in conjunction with data from an occultation event during the 1995–96 apparition. Planet. Space Sci. 47, 327–330.

Harris, A.W., 2005. Asteroid lightcurve data file. Online at http://www.minorplanetobserver.com/astlc/LC.ZIP, accessed 2006 January 25.

Hestroffer, D., Berthier, J., Descamps, P., Tanga, P., Cellino, A., Lattanzi, M., Di Martino, M., Zappalà, V., 2002a. Asteroid (216) Kleopatra. Tests of the radar-derived shape model. Astron. Astrophys. 392, 729–733.

Hestroffer, D., Descamps, P., Kaasalainen, M., Tanga, P., Torppa, J., Berthier, J., Cellino, A., Lattanzi, M., Di Martino, M., Piironen, J., Zappalà, V., 2002b. Comparison of Topographic Models for Asteroids to the HST/FGS Data. Proc. Asteroids, Comets, Meteors, 2002, ESA-SP-500, November 2002. ESA Publications Division, Noordwijk, pp. 493–496.

Holliday, B., 2001. Photometry of Asteroid 251 Sophia, 393 Lampetia, and (20898) 2002 WE147 September 2000 through January 2001. Minor Planet Bull. 28, 26–28.

Kaasalainen, M., Torppa, J., Piironen, J., 2002a. Models of twenty asteroids from photometric data. Icarus 159, 369–395.

Kryszczyńska, A., Colas, F., Berthier, J., Michałowski, T., Pych, W., 1996. CCD photometry of seven asteroids: New spin axis and shape determinations. Icarus 124, 134–140.

Lazzaro, D., Angeli, C.A., Carvano, J.M., Mothé-Diniz, T., Duffard, R., Florczak, M., 2004. S^3OS^2: The visible spectroscopic survey of 820 asteroids. Icarus 172, 179–220.

Magnusson, P., 1995. Asteroid spin vectors. Online at http://www.psi.edu/pds/archive/spin.html, accessed 2003 November 16.

Magri, C., 1995. Arm structure in normal spiral galaxies. II. Multivariate statistical analysis. Astron. J. 110, 1614–1629.

Magri, C., Ostro, S.J., Rosema, K.D., Thomas, M.L., Mitchell, D.L., Campbell, D.B., Chandler, J.F., Shapiro, I.I., Giorgini, J.D., Yeomans, D.K., 1999. Mainbelt asteroids: Results of Arecibo and Goldstone radar observations of 37 objects during 1980–1995. Icarus 140, 379–407 (Paper I).

Magri, C., Consolmagno, G.J., Ostro, S.J., Benner, L.A.M., Beeney, B.R., 2001. Radar constraints on asteroid regolith properties using 433 Eros as ground truth. Meteorit. Planet. Sci. 36, 1697–1709.

Margot, J.-L., Brown, M.E., 2003. A low-density M-type asteroid in the main belt. Science 300, 1939–1942.

Michałowski, T., 1996. Pole and shape determination for 12 asteroids. Icarus 123, 456–462.

Michałowski, T., Pych, W., Berthier, J., Kryszczyńska, A., Kwiatkowski, T., Boussuge, J., Fauvaud, S., Denchev, P., Baranowski, R., 2000. CCD photometry, spin, and shape models of five asteroids: 225, 360, 416, 516, and 1223. Astron. Astrophys. Suppl. Ser. 146, 471–479.

Millis, R.L., Dunham, D.W., 1989. Precise measurement of asteroid sizes and shapes from occultations. In: Binzel, R.P., Gehrels, T., Matthews, M.S. (Eds.), Asteroids II. Univ. of Arizona Press, Tucson, pp. 148–170.

Mitchell, D.L., Ostro, S.J., Rosema, K.D., Hudson, R.S., Campbell, D.B., Chandler, J.F., Shapiro, I.I., 1995. Radar observations of Asteroids 7 Iris, 9 Metis, 12 Victoria, 216 Kleopatra, and 654 Zelinda. Icarus 118, 105–131.

Mottola, S., Sears, W.D., Erikson, A., Harris, A.W., Young, J.W., Hahn, G., Dahlgren, M., Mueller, B.E.A., Owen, B., Gil-Hutton, R., Licandro, J., Barucci, M.A., Angeli, C., Neukum, G., Lagerkvist, C.-I., Lahulla, J.F., 1995. The slow rotation of 253 Mathilde. Planet. Space Sci. 43, 1609–1613.

Ostro, S.J., Campbell, D.B., Shapiro, I.I., 1983. Radar observations of Asteroid 1685 Toro. Astron. J. 88, 565–576.

Ostro, S.J., Campbell, D.B., Chandler, J.F., Hine, A.A., Hudson, R.S., Rosema, K.D., Shapiro, I.I., 1991. Asteroid 1986 DA: Radar evidence for a metallic composition. Science 252, 1399–1404.

Ostro, S.J., Hudson, R.S., Nolan, M.C., Margot, J.-L., Scheeres, D.J., Campbell, D.B., Magri, C., Giorgini, J.D., Yeomans, D.K., 2000. Radar observations of Asteroid 216 Kleopatra. Science 288, 836–839.

Ostro, S.J., Nolan, M.C., Margot, J.-L., Magri, C., Harris, A.W., Giorgini, J.D., 2001. Radar observations of Asteroid 288 Glauke. Icarus 152, 201–204.

Ostro, S.J., Hudson, R.S., Benner, L.A.M., Giorgini, J.D., Magri, C., Margot, J.-L., Nolan, M.C., 2002. Asteroid radar astronomy. In: Bottke, W.F., Cellino, A., Paolicchi, P., Binzel, R.P. (Eds.), Asteroids III. Univ. of Arizona Press, Tucson, pp. 151–168.

Ragazzoni, R., Baruffolo, A., Marchetti, E., Ghedina, A., Farinato, J., Niero, T., 2000. Speckle interferometry measurements of the Asteroids 10-Hygiea and 15-Eunomia. Astron. Astrophys. 354, 315–320.

Rivkin, A.S., Clark, B.E., Britt, D.T., Lebofsky, L.A., 1997. Infrared spectrophotometry of the NEAR flyby target 253 Mathilde. Icarus 127, 255–257.

Rivkin, A.S., Howell, E.S., Lebofsky, L.A., Clark, B.E., Britt, D.T., 2000. The nature of M-class asteroids from 3-μm observations. Icarus 145, 351–368.

Shinokawa, K., Takahashi, S., Ogawa, K., Yoshida, F., Minato, T., Mukai, T., Kawabata, K., 2002. Observations of photopolarimetric variation with the rotation of Asteroids, 3 Juno and 216 Kleopatra. Mem. Soc. Astron. Ital. 73, 658–661.

Snedecor, G.W., Cochran, W.G., 1980. Statistical Methods, seventh ed. The Iowa Univ. Press, Ames, IA.

Tanga, P., Hestroffer, D., Cellino, A., Lattanzi, M., Di Martino, M., Zappalà, V., 2003. Asteroid observations with the Hubble Space Telescope FGS. II. Duplicity search and size measurements for 6 asteroids. Astron. Astrophys. 401, 733–741.

Tedesco, E.F., Noah, P.V., Noah, M., Price, S.D., 2002. The Supplemental IRAS Minor Planet Survey. Astron. J. 123, 1056–1085.

Tholen, D.J., 1989. Asteroid taxonomic classifications. In: Binzel, R.P., Gehrels, T., Matthews, M.S. (Eds.), Asteroids II. Univ. of Arizona Press, Tucson, pp. 1139–1150.

Tholen, D.J., Barucci, M.A., 1989. Asteroid taxonomy. In: Binzel, R.P., Gehrels, T., Matthews, M.S. (Eds.), Asteroids II. Univ. of Arizona Press, Tucson, pp. 298–315.

Tiuri, M.E., 1964. Radio astronomy receivers. IEEE Trans. Antennas Propag. AP-12, 930–938.

Torppa, J., Kaasalainen, M., Michałowski, T., Kwiatkowski, T., Kryszczyńska, A., Denchev, P., Kowalski, R., 2003. Shapes and rotational properties of thirty asteroids from photometric data. Icarus 164, 346–383.

Tungalag, N., Shevchenko, V.G., Lupishko, D.F., 2002. Rotation parameters and shapes of 15 asteroids. Kinem. Phys. Celest. Bodies 18, 358–364.

Veverka, J., Thomas, P., Harch, A., Clark, B., Bell III, J.F., Carcich, B., Joseph, J., Chapman, C., Merline, W., Robinson, M., Malin, M., McFadden, L.A., Murchie, S., Hawkins III, S.E., Farquhar, R., Izenberg, N., Cheng, A., 1997. NEAR's flyby of 253 Mathilde: Images of a C asteroid. Science 278, 2109–2114.

Zar, J.H., 1996. Biostatistical Analysis, third ed. Prentice–Hall, Upper Saddle River, NJ.

Zimmerman, D.W., 2000. Statistical significance levels of nonparametric tests biased by heterogeneous variances of treatment groups. J. Gen. Psychol. 127, 354–364.

Further reading

Kaasalainen, M., Torppa, J., Piironen, J., 2002b. Binary structures among large asteroids. Astron. Astrophys. 383, L19–L22.

Mitchell, D.L., Ostro, S.J., Hudson, R.S., Rosema, K.D., Campbell, D.B., Vélez, R., Chandler, J.F., Shapiro, I.I., Giorgini, J.D., Yeomans, D.K., 1996. Radar observations of Asteroids 1 Ceres, 2 Pallas, and 4 Vesta. Icarus 124, 113–133.

Storrs, A., Weiss, B., Zellner, B., Burleson, W., Sichitiu, R., Wells, E., Kowal, C., Tholen, D., 1999. Imaging observations of asteroids with Hubble Space Telescope. Icarus 137, 260–268.

Thomas, P.C., Binzel, R.P., Gaffey, M.J., Zellner, B.H., Storrs, A.D., Wells, E., 1997. Vesta: Spin pole, size, and shape from HST images. Icarus 128, 88–94.